Applied Acoustics 197 (2022) 108941

Contents lists available at ScienceDirect

Applied Acoustics

journal homepage: www.elsevier.com/locate/apacoust

Taking advantage of a 3D printing imperfection in the development of sound-absorbing materials

Tomasz G. Zieliński [a,*], Nicolas Dauchez [b], Thomas Boutin [b], Mikel Leturia [b], Alexandre Wilkinson [b], Fabien Chevillotte [c], François-Xavier Bécot [c], Rodolfo Venegas [d]

[a] Institute of Fundamental Technological Research, Polish Academy of Sciences, ul. Pawińskiego 5B, 02-106 Warsaw, Poland
[b] Université de Technologie de Compiègne, Alliance Sorbonne Université, Centre de recherche Royallieu, CS 60319, 60203 Compiègne cedex, France
[c] MATELYS – Research Lab, 7 rue des Maraîchers (bâtiment B), F69120 Vaulx-en-Velin, France
[d] University Austral of Chile, Institute of Acoustics, P.O. Box 567, Valdivia, Chile

ARTICLE INFO

Article history:
Received 16 February 2022
Received in revised form 11 May 2022
Accepted 17 July 2022

Keywords:
Double porosity
Additive manufacturing
Sound absorption
Pressure diffusion
Multiscale modelling

ABSTRACT

At first glance, it seems that modern, inexpensive additive manufacturing (AM) technologies can be used to produce innovative, efficient acoustic materials with tailored pore morphology. However, on closer inspection, it becomes rather obvious that for now this is only possible for specific solutions, such as relatively thin, but narrow-band sound absorbers. This is mainly due to the relatively poor resolutions available in low-cost AM technologies and devices, which prevents the 3D-printing of pore networks with characteristic dimensions comparable to those found in conventional broadband sound-absorbing materials. Other drawbacks relate to a number of imperfections associated with AM technologies, including porosity or rather microporosity inherent in some of them. This paper shows how the limitations mentioned above can be alleviated by 3D-printing double-porosity structures, where the main pore network can be designed and optimised, while the properties of the intentionally microporous skeleton provide the desired permeability contrast, leading to additional broadband sound energy dissipation due to pressure diffusion. The beneficial effect of additively manufactured double porosity and the phenomena associated with it are rigorously demonstrated and validated in this work, both experimentally and through precise multiscale modelling, on a comprehensive example that can serve as benchmark.

1. Introduction

Modern additive manufacturing (AM) technologies [1–6] are expected to enable the development of innovative acoustic, or multi-functional, materials with optimised properties. This is evidenced by the fact that in recent years they have already been used in the research and development of a variety of new acoustic materials. Representative examples include: [3] acoustic absorbers with passive destructive interference [7], various perforated panels [8–12] and plates with complex patterns of micro-slits [13], 3D-printed periodic foams [14–17] and hollow-sphere foams [18], optimally graded porous materials [19], 3D-printed fibrous materials [20], sound-absorbing micro-lattices [21,22] and periodic structures composed of rigid micro-rods [23] or micro-bars [24], slitted sound absorbers [25], acoustic metamaterial structures and panels [26,27], acoustic metamaterials based on the Kelvin cell [28], anisotropic meta-porous surfaces [29], and even adaptable [30] and active [31] sound-absorbing composites. More examples can be found in [32]. Recently, 3D-printed porous sound absorbers have also been used to test a machine-learning approach [33], while the reproducibility of additively manufactured sound absorbers with spherical pores has been investigated through round robin tests involving various technologies, input materials, and 3D-printing devices [15,17]. The common feature of all these solutions is the use of inexpensive AM technologies and devices, characterised by relatively low resolution, which do not allow 3D-printing of microstructures (or pore networks) with dimensions comparable to those found in conventional broadband sound-absorbing materials. This results in feasible material designs that are relatively thicker when compared with conventional porous material-based solutions, and/or effective in rather narrow frequency bands, although high efficiency can often be achieved at low frequency.

The use of AM technologies in prototyping new acoustic material solutions continues [34–37], despite many technical problems as well as imperfections found in 3D printed structures, the type and size of which depends on the specific technology and input material, and even specific 3D printing devices and process

* Corresponding author.
E-mail address: tzielins@ippt.pan.pl (T.G. Zieliński).

https://doi.org/10.1016/j.apacoust.2022.108941
0003-682X/

parameters. One of the possible imperfections is microporosity, which is typical in powder bed fusion and related technologies where it is usually referred to as porosity [38–40], and can be a serious disadvantage for many applications. However, the question arises: Why not try to take advantage of the 3D printing imperfections in the development of new materials? We address this question by demonstrating that microporosity can be considered as an extremely desirable property when 3D printing acoustic materials.

This work primarily aims at showing how to take advantage of a 3D printing imperfection in the development of sound absorbing materials which exhibit double porosity effects. This is achieved by selecting AM technology, input material, and process parameters that provide a particular type of microporosity, appropriately contrasted with the designed main pore network, in the 3D-printed material. We use low-cost AM technologies to fabricate single- and double-porosity sound-absorbing materials with a relatively simple design that can be easily reproduced and serve as benchmark. The effectiveness of double-porosity acoustic materials is well known and the related physical phenomena have been theoretically explained through rigorous multiscale modelling [41–43]. The modelling was validated experimentally for real double-porosity foams [44] and granular materials [45], as well as conventional porous materials with macro-perforations [46–48]. Recently, Carbajo et al. [12] have 3D printed macro-perforated porous materials from Poly-Lactic Acid (PLA) filament using Fused Deposition Modelling (FDM) [1,2] with a simple infill pattern providing open porosities ranging from 8% to 39%, with pore sizes of at least 0.2 mm (see Table 2 and Fig. 2 in [12]) that could not be considered microporous. Our technological choice is binder jet 3D printing [3,4] and gypsum powder, providing a truly microporous skeleton in the 3D printed objects.

The outline of this paper is as follows. The following section covers the basics of multiscale modelling of acoustic wave propagation and absorption in single- and double-porosity materials with a rigid frame. Section 3 demonstrates the accuracy of this microstructure-based modelling and the benefits of additively manufactured double porosity using the example of 3D-printed materials with a cubic arrangement of spherical pores and a microporous frame (i.e. skeleton 3D-printed from powdered material) compared to the cases where the frame is impermeable thanks to: (i) impregnation, or (ii) the use of a different AM technology and input material (viz. 3-D-printing from photopolymer resin). The main observations and conclusions are summarised in Section 4.

2. Wave propagation in porous media – theoretical background

2.1. Assumptions, basic properties, and notations

In this part, the basic theoretical results and formulae related to the propagation of acoustic waves in porous media is discussed. In general, the materials under consideration consist of a skeleton, i.e. a rigid frame, and an open network of fluid-saturated pores. In double-porosity materials, which is the most relevant case in this work, the skeleton is microporous, i.e. it has an open network of fluid-saturated micropores. However, the single-porosity case (i.e. a material with a perfectly solid skeleton) is also presented because it is a useful starting point for the discussion of double-porosity materials. This is despite the fact that the physics in single- and double-porosity materials are rather different. In addition, single-porosity materials will also be studied and used for comparison in the examples. In all practical cases considered here, the saturating fluid is air.

The original works [42,43] present extensive theoretical considerations and a rigorous homogenisation technique applied to acoustics of double-porosity media. For a complete treatment of the physics of the problem under consideration – in particular, the consequences of the so-called separation of scales and various inter-scale coupling behaviours – as well as the underlying mathematical developments, the reader is directed to these works and references therein. The basic assumptions are as follows: (i) motion and forces caused by acoustic excitation are small, therefore all non-linear effects are ignored; (ii) the skeleton is assumed to be perfectly rigid, because it is either much heavier or stiffer than the fluid that saturates the pore networks; (iii) fluid compressibility is influenced by exchanges between the saturating fluid and the skeleton; (iv) a periodic elementary volume can be defined that is representative for the entire porous medium; (v) the size of the representative elementary volume (REV) is significantly smaller than the shortest wavelength of interest; (vi) the acoustically induced airflow through the pores is essentially thermoviscous, but the viscous and thermal effects can be decoupled within the fluid-saturated part of the REV, for which the macroscopic acoustic pressure is practically constant and the flow can be considered to be locally incompressible. The relatively small size of the REV provides the required scale separation, and in the case of double-porosity media, the double scale separation is ensured by the fact that the characteristic size of the REV of the microporous network is much smaller than that of the main pore network.

Following the assumption of linearity, all investigations are conducted in the harmonic regime assuming the time-harmonic convention $\exp(+\mathrm{i}\omega t)$, where i is the imaginary unit, ω is the angular frequency, and t denotes time. Obviously, $\omega = 2\pi f$, where f is the frequency.

Fig. 1 shows a typical diagram for the analysis of acoustic wave propagation and absorption in double-porosity media, which illustrates that three well separated scales are considered. The macroscale design shows a flat porous layer of thickness H backed with an air gap of thickness H_g between the back surface of the layer and a rigid wall, although a much more complex arrangement can be considered. Nevertheless, this configuration, when subject to a plane harmonic acoustic wave impinging the front surface of the porous layer at normal incidence, describes a common configuration measured in an impedance tube [49].

It is assumed that the main pore network geometry can be represented by a periodic REV Ω_p on a scale sufficiently smaller than the minimum wavelength considered. This is ensured when $\ell_p \ll L$, where ℓ_p is the size of the REV Ω_p (i.e. mesoscopic characteristic length in the case of double-porosity media, but called microscopic characteristic length in the single-porosity case) and $L = \lambda/(2\pi)$ is the macroscopic characteristic length related to the minimum expected wavelength λ in the porous medium. The REV Ω_p consists of two complementary parts: the fluid domain Ω_{pf}, which represents the main (i.e. mesoscopic) network of interconnected air-saturated pores, and the solid or microporous skeleton Ω_{ps}. Note that in the two-dimensional generic drawing shown in Fig. 1, the Ω_{ps} domain consists of separate subdomains, however, these are usually interconnected in 3D to form a compact skeleton. The interface between the fluid and skeleton domains is denoted by Γ_p. In the case of single-porosity media, Ω_{ps} is solid, and since it is also rigid, only waves that propagate in the fluid phase (associated with the fluid domain Ω_{pf}) of the material are accounted for. Hence, only the boundary Γ_p matters.

In the case of double-porosity media, the skeleton domain Ω_{ps} (or at least its part) is microporous. Here, we assume that the whole skeleton is microporous in a regular way, the microporosity is open and can be represented by a periodic REV Ω_m with size $\ell_m \ll \ell_p$ (see Fig. 1), so that the separation of scales is ensured. Similarly to the mesoscopic REV, the microscopic one is also composed of two complementary domains, viz. Ω_{mf} and Ω_{ms}. The microscopic

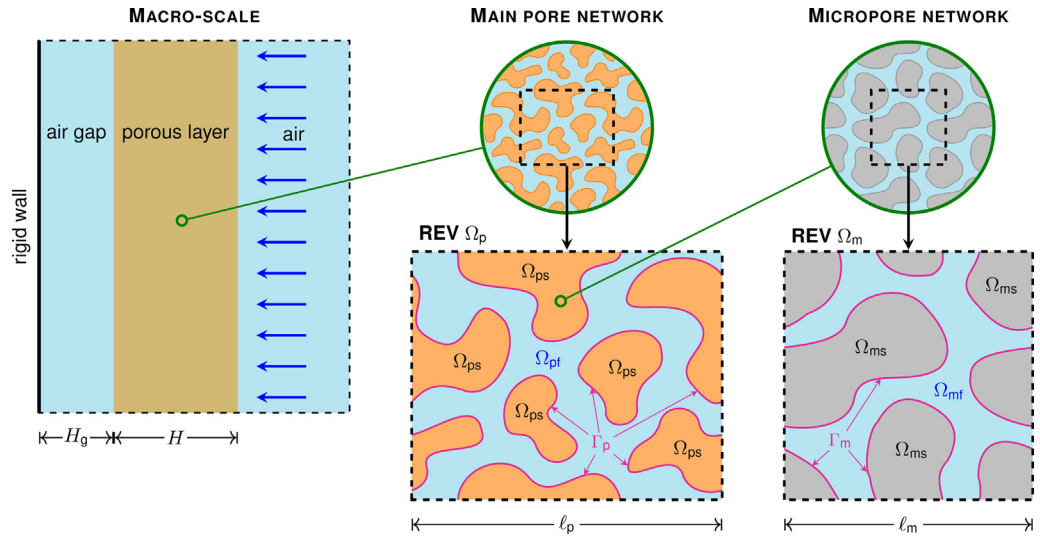

Fig. 1. Generic scheme for acoustic analysis of the double-porosity media. The periodic Ω_{ps} domain (the periodic Ω_{ms} domain) is marked in orange (grey) and additionally with appropriate labels, and can be compact in 3D. (For interpretation of the references to colour in this figure legend, the reader is referred to the web version of this article.)

fluid domain Ω_{mf} is open, compact and filled with air, while the Ω_{ms} domain is solid. The actual microporosity considered in this study is due to the specific fabrication of the skeleton using additive manufacturing in which the fine grains of the raw material are sintered or bonded together in a manner that leaves enough space between them to form an open microporous network. The grains are rigid and solid and form a compact micro-skeleton Ω_{ms}. The interface between the grains and micropore network is denoted by Γ_m.

Relevant physical parameters associated with the saturating fluid are: the mass density ϱ_0, the ambient mean pressure P_0, the heat capacity ratio (i.e. adiabatic index) γ, the dynamic viscosity η, and the Prandtl number N_{Pr}. Useful derived properties include: the kinematic viscosity $\nu = \eta/\varrho_0$ and thermal diffusivity $\nu_t = \nu/N_{Pr}$, as well as the speed of sound $c_0 = \sqrt{\gamma P_0/\varrho_0}$ and characteristic impedance $Z_0 = \varrho_0 c_0$. The values of all these parameters and properties are given in Table 1 for air under environmental conditions of the ambient mean pressure P_0, temperature T_0, and relative humidity RH, as found during the measurements made for this study.

As discussed below, the theory of wave propagation in porous media uses a dynamic generalisation of Darcy's permeability, the so-called dynamic viscous permeability [50] associated with viscous oscillating flows. Moreover, the thermal analogue of this quantity, introduced by Lafarge [51,52] and related to the temperature diffusion occurring in the porous medium, is commonly known as dynamic thermal permeability, although together with its static counterpart (i.e. static thermal permeability defined at $\omega = 0$), these are inherently direction-independent quantities, i.e. scalars, not second-order tensors. In the theory of wave propagation in double-porosity media, the so-called dynamic pressure diffusion is used as well as its static value at $\omega = 0$. These quantities have the unit of permeability and are determined on the mesoscopic representative domain of (microporous) skeleton Ω_{ps}, but in formally the same manner as the thermal permeabilities are calculated over the main pore network Ω_{pf}, see Appendix B.2. Therefore, for convenience, we may use the term permeability for all these quantities, especially when we are talking about them together, e.g. as in the "dynamic permeability" labels in Fig. 6.

2.2. Single-porosity media

Acoustic wave propagation in a single-porosity medium can be described by the effective model comprising the macroscopic mass balance equation and dynamic Darcy's law, namely

$$\nabla \cdot \mathbf{V} + \mathrm{i}\omega \mathcal{C}_p(\omega) p = 0, \qquad \mathbf{V} = -\frac{\mathcal{K}_p(\omega)}{\eta} \nabla p. \tag{1}$$

Here, $\mathbf{V}$ and p are the complex amplitudes of the flux velocity and pressure, respectively, induced by harmonic acoustic waves penetrating the air-saturated porous medium, while $\mathcal{C}_p$ is the effective compressibility of the homogenised medium and $\mathcal{K}_p$ is the dynamic viscous permeability. Here, $\mathcal{K}_p$ is a complex-valued *scalar* function of frequency. In general, the permeability is a second-order tensor, but for simplicity we assume here that the porous medium is either 'effectively' isotropic or only plane wave propagation is considered and $\mathcal{K}_p$ is the projection of the permeability tensor on the propagation direction $\mathbf{e}$. Eliminating $\mathbf{V}$ from Eqs. (1) leads to the Helmholtz equation

$$\nabla^2 p + k_p^2(\omega) p = 0, \qquad k_p(\omega) = \omega \sqrt{\frac{\eta \mathcal{C}_p(\omega)}{\mathrm{i}\omega \mathcal{K}_p(\omega)}}, \tag{2}$$

where k_p is the complex wave number in the fluid equivalent to the (homogenised) single-porosity medium. The corresponding density ϱ_p, speed of sound c_p, and characteristic impedance Z_p are complex-

Table 1
Air properties found for the ambient conditions measured during the experimental tests.

Conditions			Properties							
P_0 hPa	T_0 °C	RH %	ϱ_0 kg/m^3	c_0 m/s	Z_0 Pa·s/m	η Pa·s	γ –	N_{Pr} –	ν m^2/s	ν_t m^2/s
996.3	27.6	53	1.152	347.7	400.5	$1.846 \cdot 10^{-5}$	1.40	0.707	$1.602 \cdot 10^{-5}$	$2.266 \cdot 10^{-5}$

valued and frequency-dependent, because the equivalent fluid replaces a lossy and dispersive porous medium. They are given by

$$\varrho_{\mathrm{p}}(\omega)=\frac{\eta}{\mathrm{i}\omega\mathcal{K}_{\mathrm{p}}(\omega)},\quad c_{\mathrm{p}}(\omega)=\sqrt{\frac{\mathrm{i}\omega\mathcal{K}_{\mathrm{p}}(\omega)}{\eta\mathcal{C}_{\mathrm{p}}(\omega)}},$$
$$Z_{\mathrm{p}}(\omega)=\sqrt{\frac{\eta}{\mathrm{i}\omega\mathcal{K}_{\mathrm{p}}(\omega)\mathcal{C}_{\mathrm{p}}(\omega)}}. \tag{3}$$

These equations show that computing the complex wave number and other useful effective properties requires the dynamic permeability $\mathcal{K}_{\mathrm{p}}$ and effective compressibility $\mathcal{C}_{\mathrm{p}}$, which can be determined from the known periodic representation Ω_{p} of the main pore network, using the approach successfully applied in numerous works [53–59]. We discuss it briefly below and in Appendices A and B.

The dynamic permeability $\mathcal{K}_{\mathrm{p}}$ results from the visco-inertial effects occurring between the saturating fluid and the walls of the rigid skeleton and is determined as discussed in Appendix B.1. In practice, it can also be calculated using the scaling function (A.1), viz. $\mathcal{K}_{\mathrm{p}}(\omega)=\mathcal{X}_{\omega}(\mathcal{K}_{0\mathrm{p}},\omega_{\mathrm{vp}},\mathcal{M}_{\mathrm{vp}},\mathcal{P}_{\mathrm{vp}})$, where $\mathcal{K}_{0\mathrm{p}}\equiv\mathcal{K}_{\mathrm{p}}(0)$ and the viscous characteristic (angular) frequency ω_{vp}, shape factor $\mathcal{M}_{\mathrm{vp}}$, and low-frequency correction parameter $\mathcal{P}_{\mathrm{vp}}$ are calculated as follows

$$\omega_{\mathrm{vp}}=\frac{\phi_{\mathrm{p}}\,\nu}{\alpha_{\infty\mathrm{p}}\mathcal{K}_{0\mathrm{p}}},\quad \mathcal{M}_{\mathrm{vp}}=\frac{8\alpha_{\infty\mathrm{p}}\mathcal{K}_{0\mathrm{p}}}{\phi_{\mathrm{p}}\Lambda_{\mathrm{vp}}^{2}},$$
$$\mathcal{P}_{\mathrm{vp}}=\frac{\mathcal{M}_{\mathrm{vp}}}{4(\alpha_{0\mathrm{vp}}/\alpha_{\infty\mathrm{p}}-1)}. \tag{4}$$

Here, $\mathcal{K}_{0\mathrm{p}},\Lambda_{\mathrm{vp}},\alpha_{\infty\mathrm{p}},\alpha_{0\mathrm{vp}}$ are the static viscous permeability, viscous characteristic length, (kinematic) tortuosity, and static viscous tortuosity, respectively, determined for the main pore network as discussed in Appendix B.1.

The effective compressibility $\mathcal{C}_{\mathrm{p}}$ for a single-porosity medium is calculated as

$$\mathcal{C}_{\mathrm{p}}(\omega)=\frac{\phi_{\mathrm{p}}}{P_0}\left(1-\frac{\gamma-1}{\gamma}\frac{\Theta_{\mathrm{p}}(\omega)}{\phi_{\mathrm{p}}\,\nu_{\mathrm{t}}}\mathrm{i}\omega\right), \tag{5}$$

where Θ_{p} is the so-called dynamic thermal permeability of the porous medium. It can be determined directly (see Appendix B.2), but can also be calculated as $\Theta_{\mathrm{p}}(\omega)=\mathcal{X}_{\omega}(\Theta_{0\mathrm{p}},\omega_{\mathrm{tp}},\mathcal{M}_{\mathrm{tp}},\mathcal{P}_{\mathrm{tp}})$, where $\Theta_{0\mathrm{p}}\equiv\Theta_{\mathrm{p}}(0)$ and the thermal characteristic angular frequency ω_{tp}, shape factor $\mathcal{M}_{\mathrm{tp}}$, and low-frequency correction parameter $\mathcal{P}_{\mathrm{tp}}$ are

$$\omega_{\mathrm{tp}}=\frac{\phi_{\mathrm{p}}\,\nu_{\mathrm{t}}}{\Theta_{0\mathrm{p}}},\quad \mathcal{M}_{\mathrm{tp}}=\frac{8\Theta_{0\mathrm{p}}}{\phi_{\mathrm{p}}\Lambda_{\mathrm{tp}}^{2}},\quad \mathcal{P}_{\mathrm{tp}}=\frac{\mathcal{M}_{\mathrm{tp}}}{4(\alpha_{0\mathrm{tp}}-1)}. \tag{6}$$

Here, $\Theta_{0\mathrm{p}},\Lambda_{\mathrm{tp}},\alpha_{0\mathrm{tp}}$ are the static thermal permeability, thermal characteristic length, and static thermal tortuosity, respectively, determined for the main pore network as detailed in Appendix B.2.

2.3. Double-porosity media

As shown in Fig. 1, the skeleton of a double-porosity medium is made of a microporous material. The microporosity has to be open, but with micropores significantly smaller than the characteristic sizes of the main, i.e. mesoscopic, pore network. However, at its proper microscopic scale, the microporous material is similarly characterised by the open porosity ϕ_{m}, dynamic viscous permeability $\mathcal{K}_{\mathrm{m}}(\omega)$, and effective compressibility $\mathcal{C}_{\mathrm{m}}(\omega)$. The latter can be calculated from the dynamic thermal permeability $\Theta_{\mathrm{m}}(\omega)$ using formula (5) in which the subscript "p" is replaced by "m". The dynamic permeabilities of the microporous material, i.e. $\mathcal{K}_{\mathrm{m}}$ and Θ_{m}, can be calculated using the scaling function (A.1), provided that the viscous and thermal characteristic frequencies ω_{vm} and ω_{tm}, shape factors $\mathcal{M}_{\mathrm{vm}}$ and $\mathcal{M}_{\mathrm{tm}}$, and low-frequency correction parameters $\mathcal{P}_{\mathrm{vm}}$ and $\mathcal{P}_{\mathrm{tm}}$ have been determined for the microporous material, for example by using the formulae (4) and (6) – in which the subscript "p" is replaced by "m" – as well as the corresponding static permeabilities $\mathcal{K}_{0\mathrm{m}}$ and $\Theta_{0\mathrm{m}}$, characteristic lengths Λ_{vm} and Λ_{tm}, and tortuosities $\alpha_{\infty\mathrm{m}},\alpha_{0\mathrm{vm}}$ and $\alpha_{0\mathrm{tm}}$. On the other hand, in many practical situations the dynamic viscous permeability $\mathcal{K}_{\mathrm{m}}$ and effective compressibility $\mathcal{C}_{\mathrm{m}}$ of microporous materials are practically constant and real-valued in the frequency range of interest. In other words, below a certain frequency they are practically equal to their static values, namely

$$\mathcal{K}_{\mathrm{m}}(\omega)\approx\mathcal{K}_{0\mathrm{m}}\equiv\mathcal{K}_{\mathrm{m}}(0),\qquad \mathcal{C}_{\mathrm{m}}(\omega)\approx\mathcal{C}_{0\mathrm{m}}\equiv\mathcal{C}_{\mathrm{m}}(0)=\frac{\phi_{\mathrm{m}}}{P_0}. \tag{7}$$

In such cases, it is sufficient to determine only the static viscous permeability $\mathcal{K}_{0\mathrm{m}}$ and porosity ϕ_{m} of the microporous material, and these quantities can be measured directly, see Appendix C.1. Finally, a derived useful property is the so-called dynamic pressure diffusivity of microporous material $\mathcal{D}_{\mathrm{m}}(\omega)$ and its static counterpart $\mathcal{D}_{0\mathrm{m}}$, defined as follows

$$\mathcal{D}_{\mathrm{m}}(\omega)=\frac{\mathcal{K}_{\mathrm{m}}(\omega)}{\eta\mathcal{C}_{\mathrm{m}}(\omega)},\qquad \mathcal{D}_{0\mathrm{m}}\equiv\mathcal{D}_{\mathrm{m}}(0)=\frac{\mathcal{K}_{0\mathrm{m}}}{\eta\mathcal{C}_{0\mathrm{m}}}. \tag{8}$$

In many practical situations already mentioned above, it can be assumed that $\mathcal{D}_{\mathrm{m}}(\omega)\approx\mathcal{D}_{0\mathrm{m}}$. This happens when the thermal characteristic frequency of the microporous medium lies well above the frequency range of interest and – at the same time – is much higher than that of the main pore network.

Similarly to single-porosity media with a rigid frame, the acoustic wave propagation in double-porosity materials is governed by the corresponding macroscopic mass balance equation and dynamic Darcy's law, namely

$$\nabla\cdot\mathbf{V}+\mathrm{i}\omega\mathcal{C}_{\mathrm{db}}(\omega)p=0,\qquad \mathbf{V}=-\frac{\mathcal{K}_{\mathrm{db}}(\omega)}{\eta}\nabla p, \tag{9}$$

which can be reduced to the Helmholtz equation

$$\nabla^2 p+k_{\mathrm{db}}^2(\omega)p=0,\qquad k_{\mathrm{db}}(\omega)=\omega\sqrt{\frac{\eta\mathcal{C}_{\mathrm{db}}(\omega)}{\mathrm{i}\omega\mathcal{K}_{\mathrm{db}}(\omega)}}, \tag{10}$$

where $\mathcal{C}_{\mathrm{db}},\mathcal{K}_{\mathrm{db}}$, and k_{db} are the effective compressibility, dynamic viscous permeability, and complex wave number, respectively, determined for the fluid equivalent to the (homogenised) double-porosity medium. The effective density ϱ_{db}, speed of sound c_{db}, and characteristic impedance Z_{db} for this equivalent fluid are

$$\varrho_{\mathrm{db}}(\omega)=\frac{\eta}{\mathrm{i}\omega\mathcal{K}_{\mathrm{db}}(\omega)},\quad c_{\mathrm{db}}(\omega)=\sqrt{\frac{\mathrm{i}\omega\mathcal{K}_{\mathrm{db}}(\omega)}{\eta\mathcal{C}_{\mathrm{db}}(\omega)}},$$
$$Z_{\mathrm{db}}(\omega)=\sqrt{\frac{\eta}{\mathrm{i}\omega\mathcal{K}_{\mathrm{db}}(\omega)\mathcal{C}_{\mathrm{db}}(\omega)}}. \tag{11}$$

In the case of double-porosity media with high contrast between the permeability of the main pore network and the microporous skeleton, i.e. when $\mathcal{K}_{0\mathrm{p}}\gg\mathcal{K}_{0\mathrm{m}}$, viscous flow induced by harmonic acoustic excitation in the air is restricted mainly to the main pore network, so that the dynamic viscous permeability $\mathcal{K}_{\mathrm{db}}$ can be determined for such materials as for their single-porosity counterparts, i.e. $\mathcal{K}_{\mathrm{db}}(\omega)\approx\mathcal{K}_{\mathrm{p}}(\omega)$. On the other hand, the effective compressibility $\mathcal{C}_{\mathrm{db}}$ depends not only on the air compression and the associated heat dissipation effects in the main pore network, but also on those in the microporous skeleton. Thus, the effective compressibility of a double-porosity medium $\mathcal{C}_{\mathrm{db}}$ is a combination of the effective compressibility $\mathcal{C}_{\mathrm{p}}$ related to its main pore network and the weighted contribution of the effective compressibility $\mathcal{C}_{\mathrm{m}}$ of the microporous material constituting its skeleton. Moreover, for some double-porosity materials, i.e. the ones with appropriately high permeability contrast, an additional dissipation effect may occur due to the fact that two local acoustic pressure fields

can coexist, namely a locally constant pressure field in the more permeable pore network and a pressure field that varies locally in the less permeable micropore network, which ultimately leads to pressure diffusion that provides additional sound energy dissipation [42–48,60]. Therefore, the formula for the effective compressibility of a double-porosity material reads

$$\mathcal{C}_{\mathrm{db}}(\omega) = \mathcal{C}_{\mathrm{p}}(\omega) + \phi_{\mathrm{d}}\mathcal{C}_{\mathrm{m}}(\omega)\mathcal{F}_{\mathrm{d}}(\omega), \tag{12}$$

where ϕ_{d} is the volume fraction of the microporous domain (if the entire skeleton is microporous then $\phi_{\mathrm{d}} = 1 - \phi_{\mathrm{p}}$), and $\mathcal{F}_{\mathrm{d}}$ is the ratio of the averaged pressure locally fluctuating in the microporous domain to the pressure in the main pores, which is constant over the entire meso-pore space in the periodic cell.

The function $\mathcal{F}_{\mathrm{d}}(\omega)$ depends on two factors: (i) the relevant effective properties of the microporous material, and (ii) the size, shape and volume fraction of the microporous domain. The former contribute through the pressure diffusivity $\mathcal{D}_{\mathrm{m}}(\omega)$ of the microporous material which is the ratio (8) of the dynamic viscous permeability to the product of the effective compressibility and the dynamic viscosity of the saturating fluid. The second factor is associated with the meso-scale geometry of the microporous domain and contribute through ϕ_{d} and the dynamic pressure diffusion function $\mathcal{B}_{\mathrm{d}}(\omega)$, which is determined from the periodic domain Ω_{ps} of the microporous skeleton in formally the same way as the dynamic thermal permeability Θ_{p} is determined from the fluid domain Ω_{pf}, see Appendix B.2. Similarly, the dynamic pressure diffusion function can be approximated using the scaling function (A.1), that is $\mathcal{B}_{\mathrm{d}}(\omega) = \mathcal{X}_{\omega}(\mathcal{B}_{0\mathrm{d}}, \omega_{\mathrm{d}}, \mathcal{M}_{\mathrm{d}}, \mathcal{P}_{\mathrm{d}})$, where $\mathcal{B}_{0\mathrm{d}} \equiv \mathcal{B}_{\mathrm{d}}(0)$ is the static pressure diffusion, while the corresponding characteristic (angular) frequency ω_{d}, shape factor $\mathcal{M}_{\mathrm{d}}$, and low-frequency correction parameter $\mathcal{P}_{\mathrm{d}}$ are calculated as follows

$$\omega_{\mathrm{d}} = \frac{\phi_{\mathrm{d}}\,\mathcal{D}_{0\mathrm{m}}}{\mathcal{B}_{0\mathrm{d}}}, \quad \mathcal{M}_{\mathrm{d}} = \frac{8\mathcal{B}_{0\mathrm{d}}}{\phi_{\mathrm{d}}\,\Lambda_{\mathrm{d}}^2}, \quad \mathcal{P}_{\mathrm{d}} = \frac{\mathcal{M}_{\mathrm{d}}}{4(\alpha_{0\mathrm{d}} - 1)}. \tag{13}$$

Here, the required 'static' parameters associated with pressure diffusion, i.e. the static pressure diffusion $\mathcal{B}_{0\mathrm{d}}$, characteristic length Λ_{d}, and static tortuosity $\alpha_{0\mathrm{d}}$, are determined for the mesoscopic domain Ω_{ps} of the microporous skeleton as described in Appendix B.2. Once $\mathcal{B}_{\mathrm{d}}(\omega)$ and pressure diffusivity $\mathcal{D}_{\mathrm{m}}(\omega)$ have been determined, the function $\mathcal{F}_{\mathrm{d}}(\omega)$ can be calculated as

$$\mathcal{F}_{\mathrm{d}}(\omega) = 1 - \frac{\mathcal{B}_{\mathrm{d}}(\omega)}{\phi_{\mathrm{d}}\mathcal{D}_{\mathrm{m}}(\omega)}\mathrm{i}\omega = 1 - \frac{\mathrm{i}\omega}{\omega_{\mathrm{d}}}\frac{\mathcal{B}_{\mathrm{d}}(\omega)}{\mathcal{B}_{0\mathrm{d}}}\frac{\mathcal{D}_{0\mathrm{m}}}{\mathcal{D}_{\mathrm{m}}(\omega)}. \tag{14}$$

This is a complex-valued function, however $\mathcal{F}_{\mathrm{d}} \approx 1$ at low frequencies for $\omega \ll \omega_{\mathrm{d}}$, where pressure diffusion is negligible. The imaginary part of $\mathcal{F}_{\mathrm{d}}$ is negative and $-\mathrm{Im}\mathcal{F}_{\mathrm{d}}$ has a single peak around the characteristic frequency, i.e. for $\omega \approx \omega_{\mathrm{d}}$. The phase of $\mathcal{F}_{\mathrm{d}}$ is also negative and $-\mathrm{phase}(\mathcal{F}_{\mathrm{d}})$ is close to zero at lower frequencies, while it grows rapidly for ω approaching ω_{d}, and asymptotically becomes almost constant and maximum for $\omega \gg \omega_{\mathrm{d}}$. Moreover, $F_d(\omega \gg \omega_d) \to 0$, which reflects that the microporous skeleton behaves as perfectly impervious in such a frequency region.

For double-porosity materials with weak contrast of permeability the pressure diffusion phenomenon is not present. Then $\mathcal{F}_{\mathrm{d}} \approx 1$ (i.e. $\mathrm{Im}\mathcal{F}_{\mathrm{d}} \approx 0$ and $\mathrm{Re}\mathcal{F}_{\mathrm{d}} \approx 1$) in the whole frequency range of interest and the formula (12) can be reduced to

$$\mathcal{C}_{\mathrm{db}}(\omega) \simeq \mathcal{C}_{\mathrm{pm}}(\omega) = \mathcal{C}_{\mathrm{p}}(\omega) + (1 - \phi_{\mathrm{p}})\mathcal{C}_{\mathrm{m}}(\omega). \tag{15}$$

However, for double-porosity materials with low permeability contrast, the viscous permeability $\mathcal{K}_{\mathrm{db}}$ also depends on the fluid flow in the micropore network and therefore has to be calculated in general as discussed in [43]. Nevertheless, for some specific mesoscopic networks, i.e. with all walls parallel to the main flow and propagation direction $\mathbf{e}$ (e.g. as in meso-perforated microporous materials), the permeability $\mathcal{K}_{\mathrm{db}}$ can simply be calculated as a combination of $\mathcal{K}_{\mathrm{p}}$ and $\mathcal{K}_{\mathrm{m}}$, namely

$$\mathcal{K}_{\mathrm{db}}(\omega) \simeq \mathcal{K}_{\mathrm{pm}}(\omega) = \mathcal{K}_{\mathrm{p}}(\omega) + (1 - \phi_{\mathrm{p}})\mathcal{K}_{\mathrm{m}}(\omega). \tag{16}$$

It is evident that this formula reduces to $\mathcal{K}_{\mathrm{db}}(\omega) \approx \mathcal{K}_{\mathrm{p}}(\omega)$, if the permeability contrast is high enough, i.e. when $\mathcal{K}_{0\mathrm{p}} \gg \mathcal{K}_{0\mathrm{m}}$, which entails that $\mathcal{K}_{\mathrm{p}} \gg \mathcal{K}_{\mathrm{m}}$.

It was found that the double-porosity materials tested in this study were characterised by high permeability contrast, resulting in strong pressure diffusion effects. To show how much this diffusion affects the effective compressibility, $\mathcal{C}_{\mathrm{db}}$ calculated using Eqs. (12) and (14) is compared in some graphs below with $\mathcal{C}_{\mathrm{pm}}$ calculated using Eq. (15), i.e. as for a hypothetical (non-existent) version of the material in which the pressure diffusion is absent.

2.4. Acoustic descriptors

The main acoustic descriptor for the porous media studied in this work is the sound absorption coefficient at normal incidence determined for a porous layer of thickness H and also for such a layer backed with an air gap of thickness H_{g}, as depicted in the diagram in Fig. 1. These two macroscopic configurations, i.e. a single layer or a two-layered system, allow for analytical solutions provided that the effective properties of the fluid equivalent to the porous material are known. Essentially, the required properties are the complex wave number k_{eq} and the characteristic impedance Z_{eq} of the equivalent fluid. As discussed above, they can be determined for the single-porosity material as $k_{\mathrm{eq}}(\omega) = k_{\mathrm{p}}(\omega)$ and $Z_{\mathrm{eq}}(\omega) = Z_{\mathrm{p}}(\omega)$ using the respective formulae given in Eqs. (2) and (3), while for the double-porosity medium as $k_{\mathrm{eq}}(\omega) = k_{\mathrm{db}}(\omega)$ and $Z_{\mathrm{eq}}(\omega) = Z_{\mathrm{db}}(\omega)$ using the respective formulae given in Eqs. (10) and (11).

The sound absorption coefficient of a system subject to plane harmonic waves at normal incidence can be determined from its surface acoustic impedance Z_{s}. For the considered two-layered system shown in Fig. 1, i.e. for a (double- or single-porosity) layer backed with an air gap, the surface acoustic impedance is calculated at the front face of the porous layer as (see e.g. [61])

$$Z_{\mathrm{s}}(\omega) = Z_{\mathrm{eq}}(\omega)\frac{Z_{\mathrm{eq}}(\omega) - \mathrm{i}Z_{\mathrm{g}}(\omega)\cot\left(Hk_{\mathrm{eq}}(\omega)\right)}{Z_{\mathrm{g}}(\omega) - \mathrm{i}Z_{\mathrm{eq}}(\omega)\cot\left(Hk_{\mathrm{eq}}(\omega)\right)}, \tag{17}$$

where the impedance Z_{g} of the air gap with the thickness H_{g} depends on the wave number in the air $k_0 = \omega/c_0$ and its characteristic impedance Z_0, namely

$$Z_{\mathrm{g}}(\omega) = -\mathrm{i}Z_0\cot\left(H_{\mathrm{g}}k_0(\omega)\right). \tag{18}$$

For $H_{\mathrm{g}} = 0$, i.e. when there is no gap and the porous layer is set directly on the rigid wall, the formula for the surface acoustic impedance (17), with $|Z_{\mathrm{g}}| \to \infty$, reduces to

$$Z_{\mathrm{s}}(\omega) = -\mathrm{i}Z_{\mathrm{eq}}(\omega)\cot\left(Hk_{\mathrm{eq}}(\omega)\right). \tag{19}$$

Regardless of the configuration case, once the surface acoustic impedance Z_{s} has been determined, the acoustic reflection coefficient $\mathcal{R}$ and the sound absorption coefficient $\mathcal{A}$, can be calculated as (see e.g. [61])

$$\mathcal{R}(\omega) = \frac{Z_{\mathrm{s}}(\omega) - Z_0}{Z_{\mathrm{s}}(\omega) + Z_0}, \qquad \mathcal{A}(\omega) = 1 - |\mathcal{R}(\omega)|^2. \tag{20}$$

3. Double-porosity material with a cubic arrangement of identical spherical pores

3.1. Design and additive manufacturing of samples

Fig. 2 shows a simple periodic pore network composed of a single spherical pore with a diameter d_{sp} connected with the identical pores from the adjacent periodic cells by vertical and horizontal channels. All these channels are cylindrical and have the same

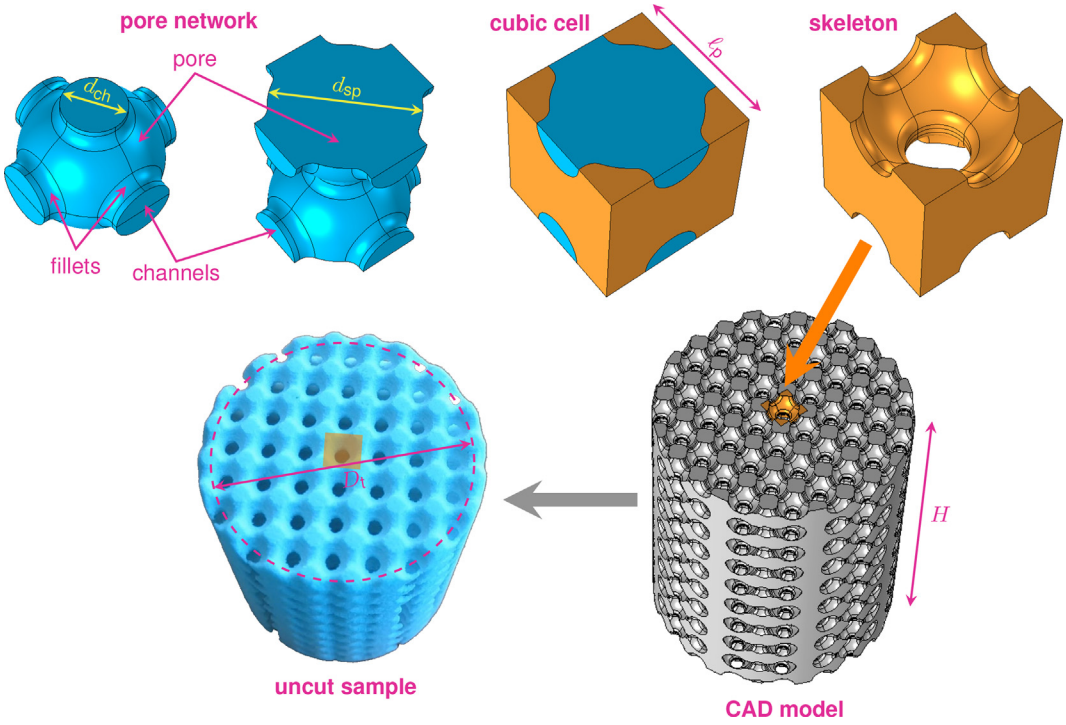

Fig. 2. Top row: periodic pore network (two views vertically shifted by half the cell size, $\frac{1}{2}\ell_p$), the corresponding representative cubic cell and skeleton. Bottom row (from right to left): CAD model of a cylindrical specimen and the resulting 3D-printed sample ($\ell_p = 4$ mm and $H = 36$ mm) with a diameter slightly larger than the required size $D_t = 29$ mm (to be cut so that it fits tightly into the 29-mm impedance tubes).

diameter d_{ch}. Each channel creates circular openings in the pores connected by it. These openings would have had sharp edges causing some numerical problems when determining the viscous characteristic length Λ_{vp} due to the local singularity at the edge [62]. To overcome these problems, the sharp edges should be rounded (filleted) at least in the numerical model [59]. In practice, the fillet radius can be arbitrarily small to ensure the numerical convergence, but a small fillet radius requires a locally very dense mesh of finite elements. Therefore, we decided to include the fillets in the design, and moreover, use a relatively large fillet radius $r_f = d_{ch}/4$, so that the rounded surface could be well reproduced by additive manufacturing, i.e. controlled by the design rather than the resolution of the 3D printer.

The smallest periodic element of the pore network Ω_{pf} together with the complementary skeletal part Ω_{ps} form a periodic cube cell Ω_p of size ℓ_p as shown in Fig. 2. The diameters of pores and channels are directly related to the cell size, viz. $d_{sp} = 0.9\ell_p$ and $d_{ch} = 0.4\ell_p$. The computer-aided design (CAD) model of the periodic skeleton cell (marked in orange in Fig. 2) was used to generate the geometry of cylindrical samples of such designed porous layers of thickness H. Two cell sizes were considered, viz. $\ell_p = 3$ mm and $\ell_p = 4$ mm, as well as two different sample heights (i.e. layer thicknesses) in both of these cases, viz. $H = 36$ mm and $H = 48$ mm, which gives four CAD models of porous samples. In order to generate them, the skeleton cell was virtually multiplied and arranged in three-dimensional arrays of $N \times N \times N_z$ cells, where $N = 11$ for $\ell_p = 3$ mm and $N = 9$ for $\ell_p = 4$ mm, while the number of cells in the vertical direction N_z is determined directly from the cell size and the assumed layer thickness, viz. $N_z = H/\ell_p$, which means that $N_z = 9, 12$, or 16. Then, cylinders with a diameter of 31 mm and height $H = 36$ mm or 48 mm were virtually cut out from the cuboidal arrays of cells. It that way, four CAD models of porous samples were generated (one of them is depicted in grey in Fig. 2). Their diameter was by 2 mm larger than the required sample diameter $D_t = 29$ mm (see photo of *uncut* sample in Fig. 2), so that the samples could be precisely cut to fit the 29-mm measurement tubes perfectly and avoid measurement errors incurred by air–gaps around the samples [63,49].

The CAD models were used to produce twelve porous samples (see Fig. 3) in two additive manufacturing technologies, viz. Color Jet Printing (CJP) – a binder jet 3D printing technology [3,4], and Stereolithography (SLA) [5,6] based on photopolymerisation. In the case of CJP technology, samples were 3D printed from gypsum-based powder, or more specifically from Calcium sulfate hemihydrate (a.k.a. bassanite) powder bound with butyrolactam (a.k.a. 2-Pyrrolidone), using *3D Systems ProJet 160* printer. Relevant properties of the gypsum powder are discussed in Appendix C.1. Four pairs of CJP samples were manufactured (with cell sizes $\ell_p = 3$ mm or 4 mm, and heights $H = 36$ mm or 48 mm, respectively), and one of the samples from each pair was additionally impregnated with cyanoacrylate to close the micropores in the skeletons of these samples. In that way, each of the four pairs contains a single-porosity CJP-impregnated sample (see the middle row in Fig. 3 and a double-porosity CJP sample (see the top row in Fig. 3). In the case of SLA technology, single-porosity samples (see the bottom row in Fig. 3) were produced at once from a photopolymer resin using *Formlabs Form 3B* printer. The relatively low viscosity of the resin (0.93 Pa·s in 25°C) facilitated the removal of resin residues from the pore network. As mentioned above, the diameters of all 3D printed samples, initially equal to 31 mm, were precisely cut with a lathe to perfectly fit into a 29-mm impedance tube. This procedure was adopted for all samples.

3.2. Examination of the actual geometry

The impact of AM processes on the performance of acoustic materials can be very significant as even small geometric deviations and imperfections matter and are related to the technology and input material used [15–17]. The quality and actual geometry of the pore network of the CJP and SLA samples were examined

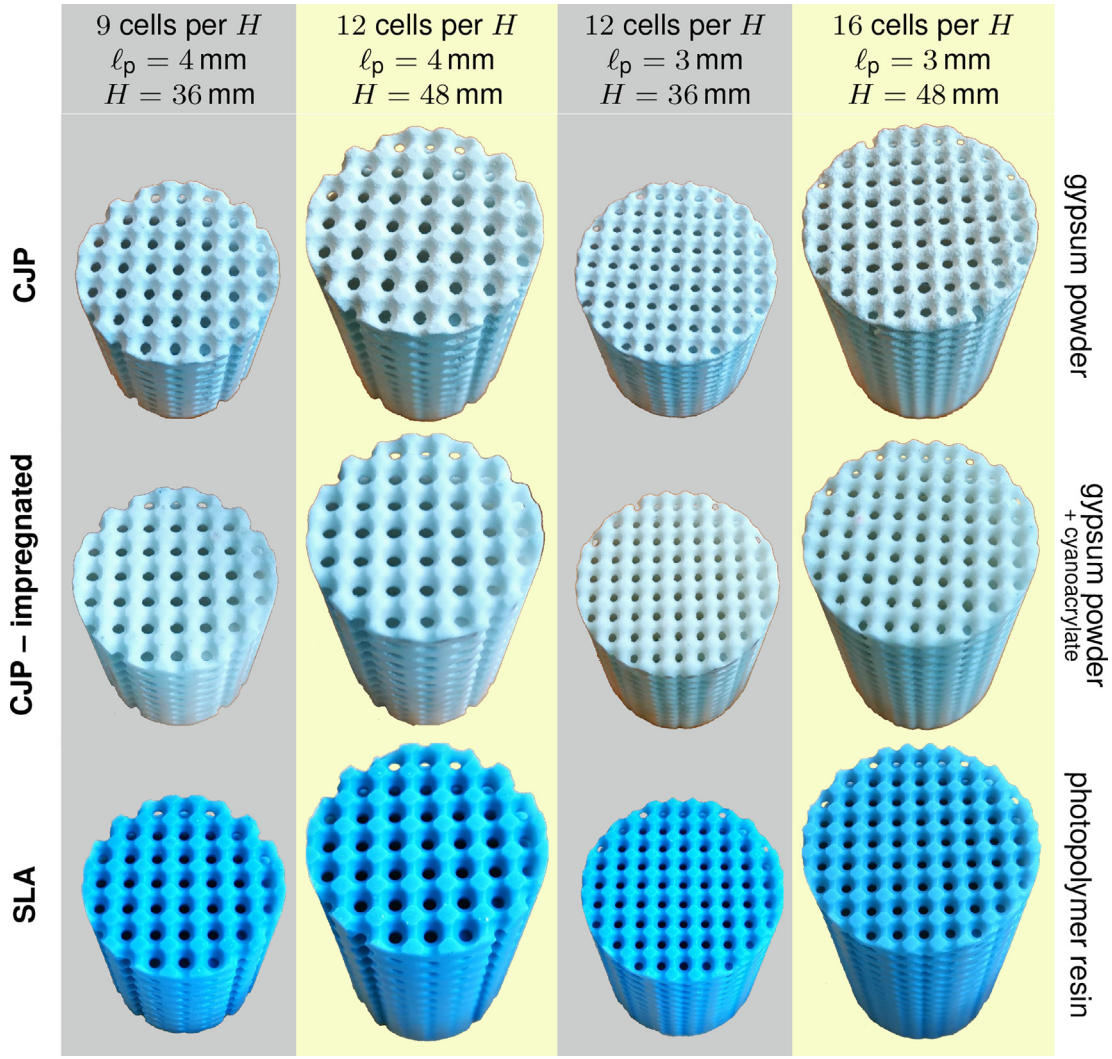

Fig. 3. Additively manufactured samples.

under a microscope (60× magnification was used). Some of the calibrated microscope photographs are shown in Fig. 4, on which the actual radii of pores and channels are measured (see the values assigned to 'r'). As expected, the actual diameters of pores and channels are slightly different than their nominal sizes in CAD models, cf. the respective values listed in Table 2. Although the same CAD models were used to produce the CJP and SLA samples, the actual pore and channel sizes, as well as the quality of the 3D printed samples, depend on the 3D printing technology and input material used, as it is clearly seen in Fig. 4.

Fig. 4 shows microscope photographs of non-impregnated and impregnated CJP samples, as well as the corresponding SLA samples. In each case two photographs are presented, i.e. for the cell sizes of 3 mm and 4 mm, respectively. The shapes, sizes, and overall quality of the impregnated CJP samples are practically the same as their non-impregnated counterparts, although the surfaces of the impregnated samples are smoother. The observed quality of CJP samples is mediocre or even poor in the case of 3 mm cell (see Fig. 4 a and c), where the cross-section of the channel appears to be somewhat elliptical rather than circular (the average estimated radius of 0.55 mm is approximative). On the other hand, the quality can be considered good for the CJP sample with 4 mm cells (see Fig. 4 b and d), where the channel is round with an easy-to-measure radius of 0.75 mm. Nevertheless, the actual diameters of the channels are in both cases smaller by 0.1 mm than their nominal sizes in the CAD models used for 3D printing: compare d^*_{ch} with the corresponding d_{ch} for CJP 3 and CJP 4 in Table 2. Finally, in both cases, it is more difficult to measure the size of spherical pores due to the not very sharp (in the photographs, but also in reality, because the removal of powder residues damaged sharp constrictions) or even indistinct edges of the skeleton made of gypsum powder. Therefore, the proposed estimations are approximate. It is characteristic, however, that the actual diameters of these quasi spherical pores seem to be larger (by about 0.2 mm for CJP 3 or 0.3 mm CJP 4) than their nominal values: compare d^*_{sp} with the corresponding d_{sp} for CJP 3 and CJP 4 in Table 2.

The quality of SLA samples is excellent regardless of the cell size (see Fig. 4 e and f): the channels are round and smooth with a circular cross section, the shape of the spherical pore is precisely mapped, and it is easy to accurately measure the actual pore and channel sizes. The respective values listed in Table 2 for the SLA samples show that the actual pore diameters are 0.04 mm smaller than their nominal (i.e. designed) values, while the actual channel diameters are smaller by 0.10 mm than their nominal values.

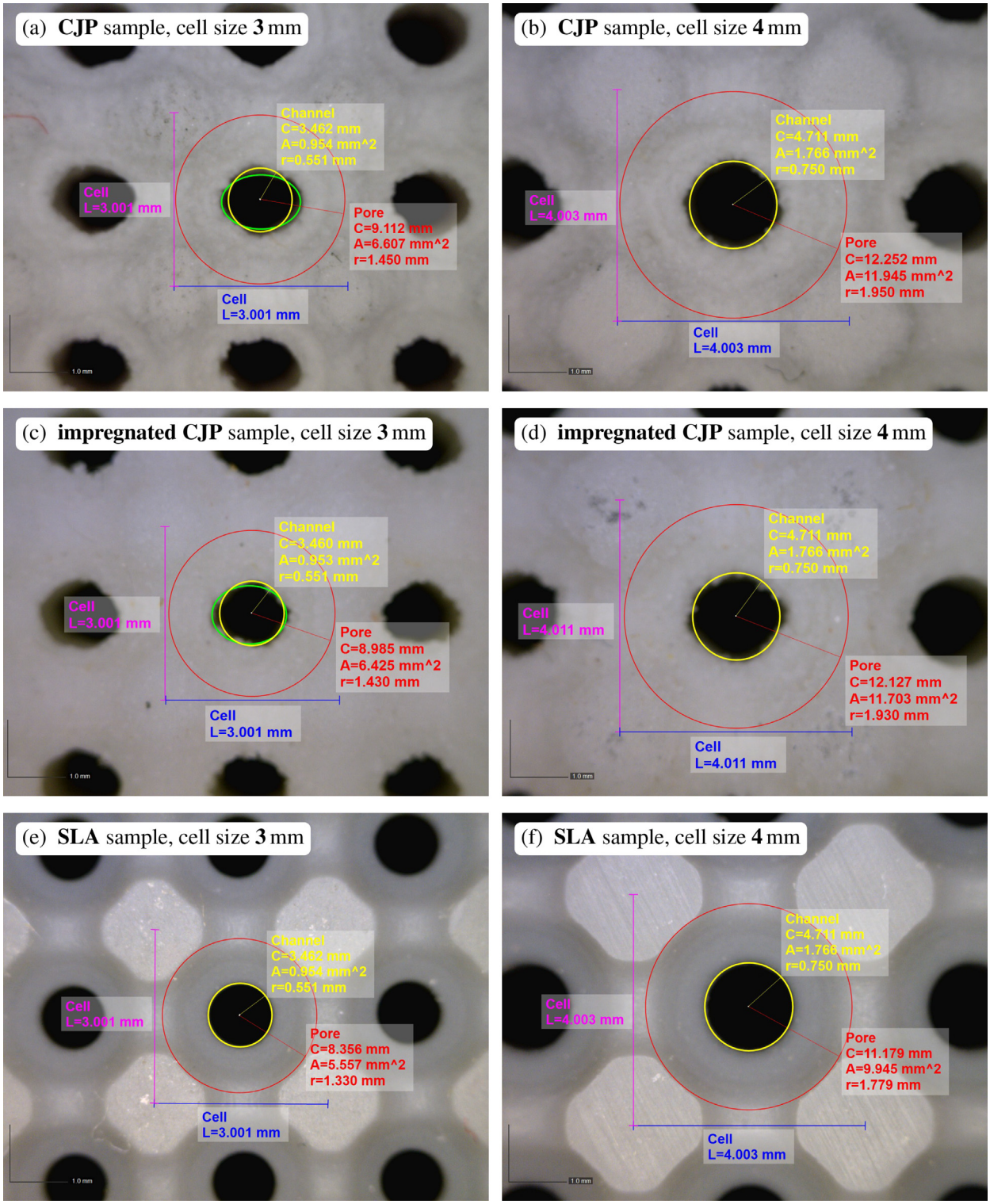

Fig. 4. Microscope examination of 3D printed samples (C, A, and r in the photographs represent the circumference, area, and radius of the pore or channel cross-section, respectively).

3.3. Mutli-scale modelling

The actual values of diameters listed in Table 2 (note that the corrected fillet radii are $r_{\mathrm{f}}^{*} = 0.15 d_{\mathrm{ch}}^{*}$ for CJP samples of inferior quality, and $r_{\mathrm{f}}^{*} = 0.25 d_{\mathrm{ch}}^{*}$ for SLA samples of excellent quality, where the rounded surface is very well reproduced as shown in Fig. 4 e and f) were used to generate updated periodic cells required for calculations at the mesoscopic scale. A typical correction for SLA samples is illustrated in the graphic in the upper left corner of Fig. 5, where the yellow part shows the difference between the design and the actual periodic pore network present in the samples 3D printed in SLA technology. In that case, the difference is simply removed. The fragments removed in the case of CJP samples look different and, moreover, in this case there are also larger fragments added due to the fact that the pore sizes in these samples are actually slightly larger than in the design. In both

Table 2
Pore network sizes: nominal (i.e. designed) and actual values.

Sample		Nominal sizes			*Actual values		
Type	ℓ_p mm	$d_{sp} = 0.9\ell_p$ mm	$d_{ch} = 0.4\ell_p$ mm	$r_f = 0.25d_{ch}$ mm	d^*_{sp} mm	d^*_{ch} mm	r^*_f mm
CJP	3	2.70	1.20	0.30	~2.9	~1.1	0.165
SLA	3	2.70	1.20	0.30	2.66	1.10	0.275
CJP	4	3.60	1.60	0.40	~3.9	1.50	0.225
SLA	4	3.60	1.60	0.40	3.56	1.50	0.375

ℓ_p – cubic cell size d_{sp} – spherical pore diameter d_{ch} – channel diameter r_f – fillet radius.

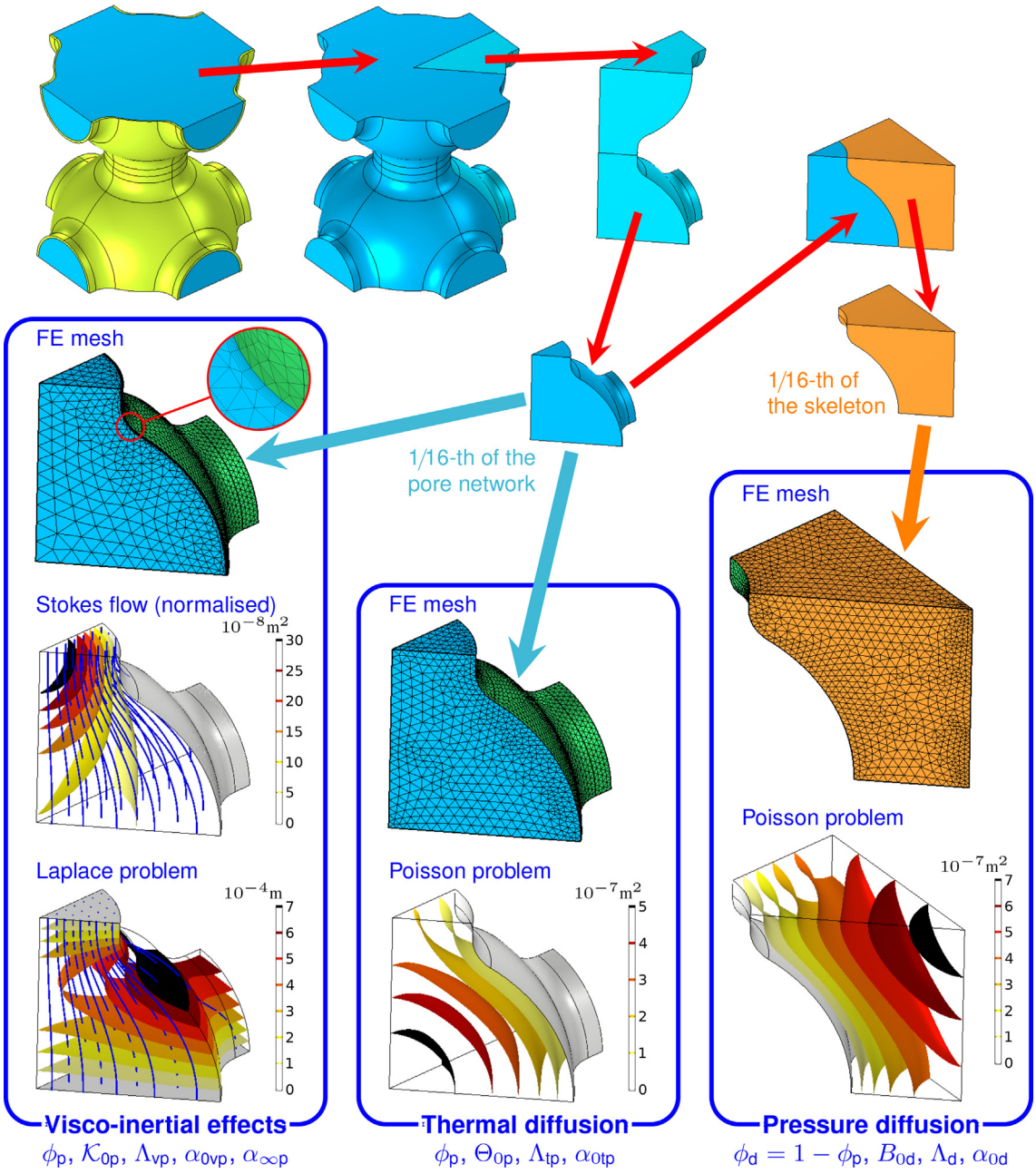

Fig. 5. Pore network size correction (yellow parts are removed in the process) and symmetrical slicing, followed by finite-element calculations of macro-parameters related to micro-scale phenomena. (For interpretation of the references to colour in this figure legend, the reader is referred to the web version of this article.)

cases, the consequence is that the porosities associated with the corrected (i.e. updated) pore networks differ by a few percent from the designed value of 44.1%. They are slightly smaller for SLA samples, but larger for CJP samples due to the larger actual pore sizes: compare the respective values for ϕ_p in Table 3. It should be noticed that the calculated porosities of the main pore networks

Table 3
Macro-parameters calculated for 3D printed materials, i.e. double-porosity samples (technology CJP) and resin samples (technology SLA) with the periodic cell size $\ell_p = 3$ mm or 4 mm.

Sample		Visco-inertial effects					Thermal effects				Pressure diffusion			
Type	ℓ_p mm	ϕ_p %	$\mathcal{K}_{0p}$ 10^{-8}m^2	Λ_{vp} mm	α_{0vp} –	$\alpha_{\infty p}$ –	ϕ_p %	Θ_{0p} 10^{-8}m^2	Λ_{tp} mm	α_{0tp} –	ϕ_d %	$\mathcal{B}_{0d}$ 10^{-8}m^2	Λ_d mm	α_{0d} –
CJP	3	49.6	1.36	0.631	2.70	1.92	49.6	7.72	1.15	1.37	50.4	7.10	1.17	1.35
SLA	3	41.7	1.10	0.623	2.64	1.91	41.7	5.38	1.04	1.39	–	–	–	–
CJP	4	50.7	2.66	0.862	2.65	1.88	50.7	14.4	1.56	1.36	49.3	11.9	1.52	1.36
SLA	4	42.3	2.10	0.850	2.59	1.87	42.3	9.86	1.40	1.38	–	–	–	–

of samples manufactured from gypsum powder, i.e. $\phi_p = 0.496$ for CJP 3 and $\phi_p = 0.507$ for CJP 4, agree very well with the respective values of 0.49 and 0.51, determined by the experimental characterisation of the impregnated CJP samples (see Table C.2 in Appendix C.2). These porosities (especially in the case of CJP 4) are only slightly below the value of 0.525 obtained from direct measurements of the average open porosity of impregnated CJP samples (see Appendix C.1). The difference can be explained by the highly probable assumption that even after impregnation the CJP samples may still have a very thin irregular layer of microporosity on the surface of their skeletons, which can increase the measured open porosity.

Fig. 5 illustrates the entire procedure of numerical calculations on a REV of the mesoscopic pore network. The periodic REV

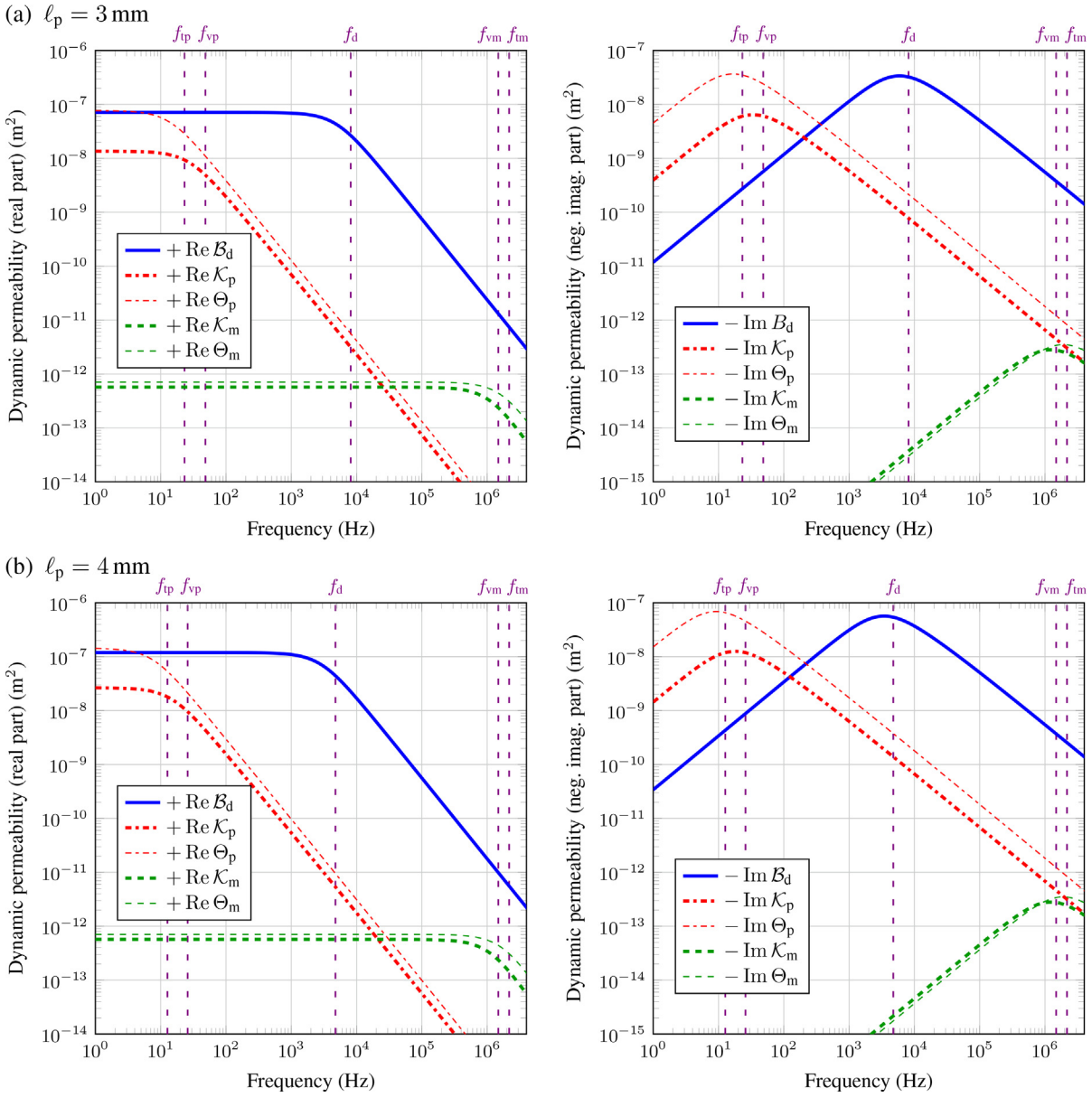

Fig. 6. Dynamic permeabilities related to the visco-inertial effects, thermal diffusion and pressure diffusion in the examined double-porosity medium (i.e. assuming the pore networks of CJP samples) with a periodic cell size of: (a) $\ell_p = 3$ mm, (b) $\ell_p = 4$ mm.

considered in this study is very regular and has six planes of symmetry. Therefore, after an updated REV is generated, its smallest representative segment (1/16-th of the pore network inside the periodic cell) can be virtually cut out by the symmetry planes. The segment is meshed and used for solving the relevant scaled Stokes flow and Laplace problem (as discussed in Appendix B.1), as well as the Poisson problem (as discussed in Appendix B.2), using the finite element method. As shown in the detail of one mesh graphic in Fig. 5, the finite element mesh used for analysis of the Stokes flow has several thin boundary layers to ensure the convergence and accuracy of the solution; these are not required when solving other problems.

For each problem, in addition to the appropriate boundary conditions discussed in Appendix B and applied on the skeleton-fluid interface Γ_p (marked in green in Fig. 5), the symmetric and antisymmetric boundary conditions are applied on the planes of symmetry and antisymmetry of the pore network segment. Notice that the lateral planes of the pore network segment are always its symmetry planes, while the antisymmetry planes are only the top and bottom surfaces of the segment for the Stokes flow and Laplace problem, assuming that the propagation direction $\mathbf{e}$ (see Appendix B.1) is vertical, but not for the Poisson problem where these surfaces are also planes of symmetry. When the scaled (i.e. normalised) Stokes flow has been solved (see Fig. 5), the static viscous permeability $\mathcal{K}_{0p}$ and static viscous tortuosity α_{0vp} are calculated using formulae (B.6), whereas from the solution of the Laplace problem (see Fig. 5), the kinematic tortuosity $\alpha_{\infty p}$ and viscous characteristic length Λ_{vp} are determined using formulae (B.11). These parameters, together with the porosity ϕ_p, allow to accurately approximate the dynamic viscous permeability $\mathcal{K}_p(\omega)$ for the main pore network saturated with fluid (i.e. air) with kinematic viscosity ν, using the scaling function (A.1) and formulae (4). The values of these parameters, computed for the updated periodic geometries associated with the actual samples 3D printed in technologies CJP and SLA, are listed in Table 3 as macro-parameters related to visco-inertial effects.

Similarly, macro-parameters related to thermal effects, found directly from the pore network geometry (ϕ_p and Λ_{tp}) and from the Poisson problem solution (Θ_{0p} and α_{0tp}), see Appendix B.2 and formulae (B.16), are also listed in Table 3 for all samples. These parameters, along with thermal diffusivity of air ν_t and formulae (6), allow to determine the dynamic thermal permeability $\Theta_p(\omega)$, using the scaling function (A.1). On the other hand, the macro-parameters related to pressure diffusion are given in Table 3 for the double-porosity CJP samples only. These are the volume fraction ϕ_d and characteristic length Λ_d of the skeleton, determined from its geometry, as well as static parameters $\mathcal{B}_{0d}$ and α_{0d}, determined from the corresponding Poisson problem solution, see Appendix B.2 and formulae (B.17).

Now, the dynamic pressure diffusion $\mathcal{B}_d(\omega)$ can be determined for these samples using the scaling function (A.1) and formulae (13), along with the static pressure diffusivity $\mathcal{D}_{0m} = \frac{P_0}{\eta}\frac{\mathcal{K}_{0m}}{\phi_m} = 7.21 \cdot 10^{-3}\,\mathrm{m^2/s}$ determined for the microporous material (see Appendix C.1, where the microporosity and static viscous permeability are determined as $\phi_m = 0.426$ and $\mathcal{K}_{0m} = 5.7 \cdot 10^{-13}\,\mathrm{m^2}$, respectively) and the ambient conditions measured during the acoustic testing (see data P_0 and η in Table 1). Finally, note that the macro-parameters calculated for visco-inertial and thermal effects are compared in Appendix C.2 with their counterparts characterised experimentally for single-porosity samples.

Fig. 6 presents the frequency variation of dynamic functions $\mathcal{K}_p, \Theta_p$, and $\mathcal{B}_d$, computed for the CJP samples of both cell sizes. For comparison, the graphs also show dynamic permeabilities $\mathcal{K}_m$ and Θ_m found for microporous material made of glued grains of gypsum powder with an effective diameter of 20 µm (see Appendices C.1 and D). The values of the characteristic frequencies f_{vp}, f_{tp}, and f_d (also f_{vm} and f_{tm}), calculated from their angular counterparts and related to viscous effects, and thermal and pressure diffusions, are marked on the graphs to demonstrate that the peak in the imaginary part of each dynamic permeability is determined by their characteristic frequencies. In particular, the computed characteristic frequencies associated with the pressure diffusion are $f_d = \frac{\omega_d}{2\pi} = 8.14\,\mathrm{kHz}$ for $\ell_p = 3\,\mathrm{mm}$, and $f_d = 4.75\,\mathrm{kHz}$ for $\ell_p = 4\,\mathrm{mm}$. The corresponding functions $\mathcal{F}_d$, calculated for both cell sizes using formula (14), are shown in Fig. 7 to illustrate that their magnitudes and phases become significantly different than zero at frequencies above 1 kHz, with the maximum magnitude slightly below f_d and the largest phase shift settling slightly above f_d. This shows that the effect of pressure diffusion will occur over a wide frequency range around the characteristic frequency.

The real and imaginary parts of the effective compressibility $\mathcal{C}_{db}(\omega)$ of the double-porosity material, calculated by formula (12) and normalised by dividing by the isothermal air compressibility $1/P_0$, are shown in Fig. 8. They are compared with the normalised counterparts $\mathcal{C}_p P_0, \mathcal{C}_m P_0$, and $\mathcal{C}_{pm} P_0$, associated with, respectively: the main pore network, the microporous material, and a virtual double-porosity material in which the effect of

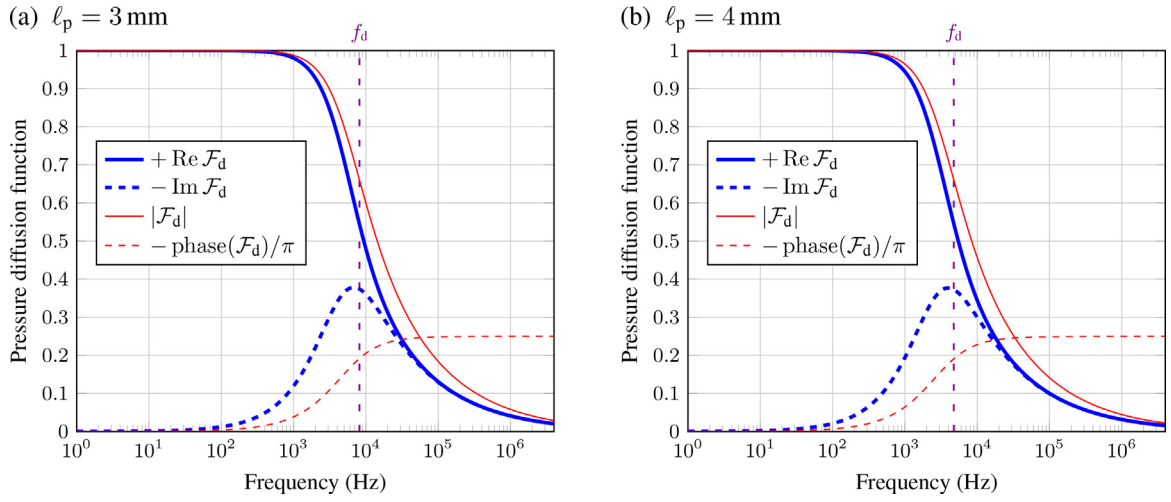

Fig. 7. Function $\mathcal{F}_d$ (its real and imaginary parts, magnitude and normalised phase) for the examined double-porosity medium, i.e. CJP samples with a periodic cell size of: (a) $\ell_p = 3\,\mathrm{mm}$, (b) $\ell_p = 4\,\mathrm{mm}$.

pressure diffusion has been artificially eliminated. In the latter case, the corresponding effective compressibility $\mathcal{C}_{\mathrm{pm}}(\omega)$ is calculated by Eq. (15), obtained for $\mathcal{F}_{\mathrm{d}}(\omega) \equiv 1$. Let us also recall that the effective compressibility $\mathcal{C}_{\mathrm{p}}(\omega)$ is calculated using Eq. (5), and the compressibility $\mathcal{C}_{\mathrm{m}}(\omega)$ using the same formula, but after replacing the index 'p' with 'm'. When comparing the curves, it is direct to see that the negative imaginary part of $\mathcal{C}_{\mathrm{db}}$ has two peaks. The first is related to the thermal effects occurring in the main pore network at the frequency f_{tp}. Below and around this characteristic frequency, the curve for $\mathrm{Im}\mathcal{C}_{\mathrm{db}}$, calculated in the case of double porosity, is similar to the $\mathrm{Im}\mathcal{C}_{\mathrm{p}}$ curve obtained for the corresponding single-porosity material. The second peak is due to the pressure diffusion at the frequency f_{d}.

3.4. Sound absorption: predictions vs. measurements

The dynamic permeabilities of the investigated single-porosity, double-porosity, and microporous materials, i.e. $\mathcal{K}_{\mathrm{p}}, \mathcal{K}_{\mathrm{db}}$, and $\mathcal{K}_{\mathrm{m}}$, respectively, together with the effective compressibilities $\mathcal{C}_{\mathrm{p}}, \mathcal{C}_{\mathrm{db}}$, and $\mathcal{C}_{\mathrm{m}}$, respectively, allow to calculate the corresponding complex wave numbers $k_{\mathrm{eq}} = \omega\sqrt{\frac{\eta\,\mathcal{C}_{\mathrm{eq}}}{\mathrm{i}\omega\mathcal{K}_{\mathrm{eq}}}}$, and characteristic impedances $Z_{\mathrm{eq}} = \sqrt{\frac{\eta}{\mathrm{i}\omega\,\mathcal{K}_{\mathrm{eq}}\,\mathcal{C}_{\mathrm{eq}}}}$, where eq='p', 'db', and 'm', respectively. These can be used to determine the surface acoustic impedance Z_{s} for a layer of the considered porous material of thickness H, backed by a rigid wall – using formula (19), or with an air gap of known thickness H_{g} between the rigid wall and the porous layer – in that case using formula (17). For both configuration cases (i.e. with or without the air gap), the sound absorption is determined using Eqs. (20).

Figs. 9 and 10 show the sound absorption curves calculated as discussed above and measured in an impedance tube [49] for the CJP samples with double porosity and for the single-porosity SLA samples. Experimental results for the impregnated, i.e. single-porosity CJP samples, are also presented as they differ slightly from the absorption curves measured for the SLA samples. However, their predictions are very similar to those obtained for the SLA samples and were not included in the graphs for the sake of clarity. In addition, each of the graphs also shows the sound absorption calculated for a homogeneous microporous layer with the same

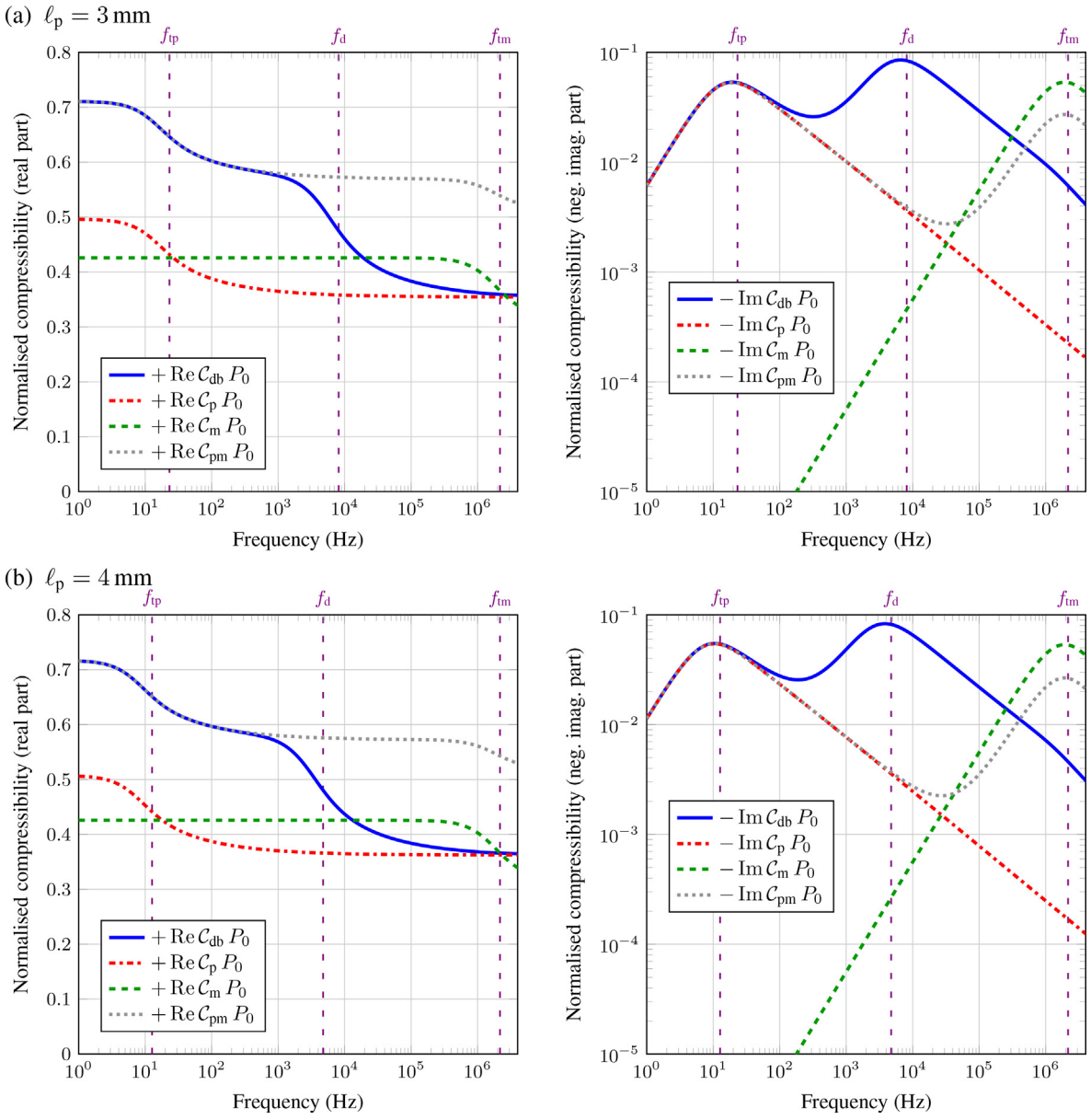

Fig. 8. Normalised effective compressibilities of the examined single- and double-porosity media with a periodic cell size of: (a) $\ell_{\mathrm{p}} = 3\,\mathrm{mm}$, (b) $\ell_{\mathrm{p}} = 4\,\mathrm{mm}$.

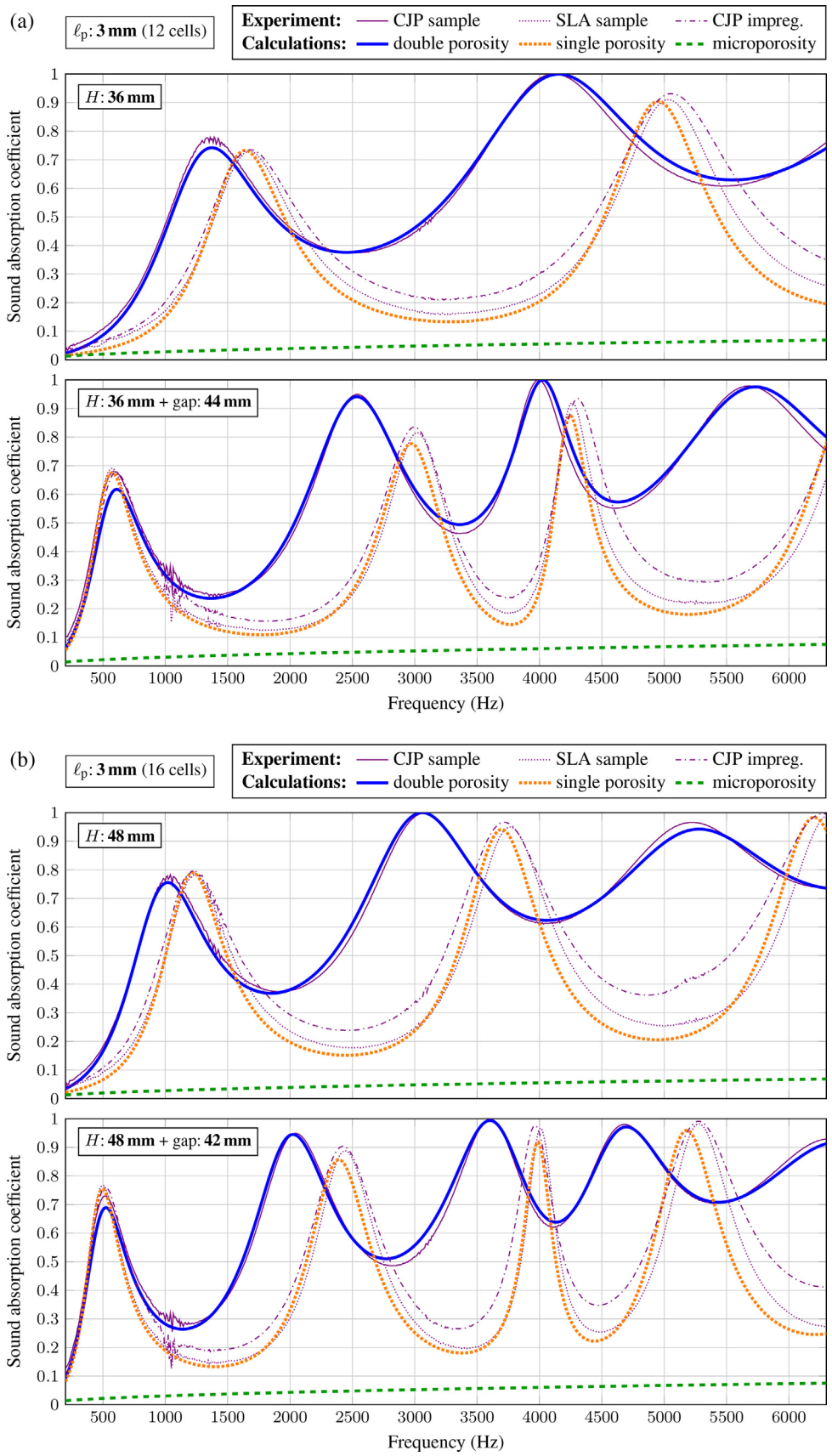

Fig. 9. Predicted and measured sound absorption for single- and double- porosity samples (backed with a rigid wall or an air gap) with a periodic cell size of $\ell_p = 3$ mm and a height of: (a) $H = 36$ mm, and (b) $H = 48$ mm.

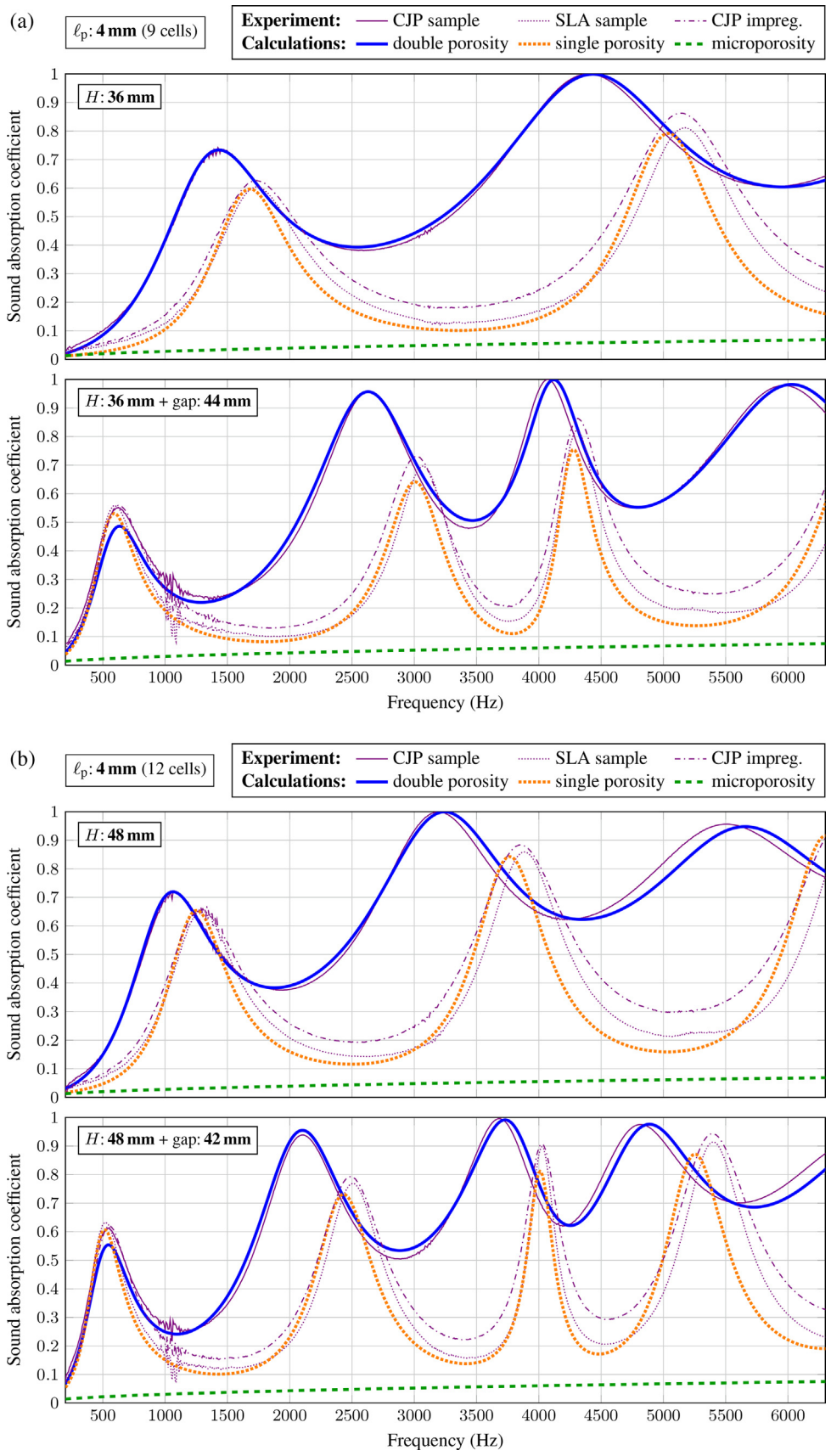

Fig. 10. Predicted and measured sound absorption for single- and double- porosity samples (backed with a rigid wall or an air gap) with a periodic cell size of $\ell_p = 4$ mm and a height of: (a) $H = 36$ mm, and (b) $H = 48$ mm.

thickness H as the height of the 3D-printed samples. This absorption is very poor, below 0.1 in the entire frequency range, so the corresponding experimental curves are not included.

The results obtained for samples with a cell size of 3 mm and 4 mm are shown in Figs. 9 and 10, respectively. There are two sample heights for each cell size, viz. $H = 36$ mm (which means twelve 3-mm cells per sample height, or nine 4-mm cells) or $H = 48$ mm (i.e. sixteen 3-mm cells or twelve 4-mm cells per sample height). Therefore, the corresponding absorption curves can also be compared between the graphs as they are obtained for materials of the same thickness. The general observations and conclusions are the same in all cases. In particular, there is an overall good agreement between measurements and numerical predictions, although the latter are computed from idealised REV geometries with smooth surfaces and may often underestimate sound absorption, especially between peaks. On the other hand, the experimental results may be affected by measurement noise. We know, however, that the absorption curves are inherently smooth and any small local fluctuations, e.g. as the ones observed around 1.1 kHz in the lower graph of each pair of graphs in Figs. 9 and 10, are measurement artifacts.

The sound absorption measured for the SLA samples confirms the model-based predictions very well, cf. the corresponding dotted curves in Figs. 9 and 10. This is due to the high quality of these samples (see Fig. 4 e and f), which allowed for accurate geometry updating and modelling. Sound absorption measured for the impregnated CJP samples (plotted as dash-dotted curves in Figs. 9 and 10) is slightly higher between peaks than in the case of the smooth SLA samples. Similar differences have already been observed for acoustic materials fabricated with different AM technologies [15–17] and can be attributed to the surface roughness [64,65]. Nevertheless, the absorption curves are similar for samples with the same cell size and height, since the impregnated CJP samples also have a single-porosity network with channels approximately the same diameter as in the SLA samples. Although the pores of the CJP samples are slightly larger, this proved to be less important and the predictions calculated for the single-porosity CJP samples are in fact very similar to those calculated for the SLA samples, therefore they are not shown in the plots for the sake of clarity. The similarity of the predictions for the respective single-porosity samples results from the fact that the actual channel diameters used in the calculations were identical for both cases, CJP and SLA, and this parameter has a strong impact on the viscous permeability and characteristic length. This is in line with similar findings, e.g. for conventional acoustic foams, where the most influential microstructural parameter having a dominant effect on the viscous permeability is the throat size according to Refs. [54,66], or alternatively, the strut length [67].

An excellent agreement has been found between the calculated and measured sound absorption for the double-porosity CJP samples, shown in Figs. 9 and 10 as thick blue and thin violet continuous curves, respectively. The nature of these absorption curves is completely different from the (dotted and dashed-dotted) curves obtained for the case of single porosity, namely: all absorption peaks have been shifted to lower frequencies and the overall absorption between them is much higher. This is caused by pressure diffusion, which significantly increases sound absorption and thus weakens any effects from minor geometric imperfections. Figs. 9 and 10 also show dashed green curves of the extremely low absorption calculated for microporous layers with the same thicknesses (i.e. $H = 36$ mm or $H = 48$ mm) as the heights of the 3D-printed samples, which means that the increase in absorption achieved in the samples with double porosity is mainly due to pressure diffusion. Important is also the following observation. For each double-porosity sample backed by a rigid wall, the first absorption peak is in the frequency range where pressure diffusion occurs, i.e. where the imaginary parts and phases of the corresponding $\mathcal{F}_d$ functions are significantly different than zero (see Fig. 7). However, when the sample is backed with an air gap (in the considered cases: 44 mm or 42 mm thick), its first absorption peak is shifted to a much lower frequency (around 700 Hz or 500 Hz) where there is no significant pressure diffusion, and therefore this peak is very similar to that obtained in the respective single-porosity case, while the pressure diffusion effect continues to enhance the second and subsequent absorption peaks. Note that we chose to use gaps that could be set very precisely. For samples with a height of 36 mm, it is practical and easier to precisely set the air gap of 44 mm (than a gap of, e.g. 40 mm or 50 mm), because the total thickness of such a configuration is exactly 8 cm, and the marks on the impedance tube plunger are every 1 cm. For the same reasons, i.e. to ensure high precision in experimental testing, the air gap of 42 mm is set behind the samples with a height of 48 mm, because the total thickness is then 9 cm, which is marked on the plunger.

4. Conclusions

We have shown in this paper that microporosity, typical to some AM technologies, but at the same time only achievable in a useful form with certain input materials and process parameters, can be regarded as an extremely desirable property in the development of innovative acoustic materials. This is because double-porosity structures with designed, optimised networks of main pores appropriately contrasted with micropores can be easily produced. Thanks to this, additional dissipation phenomena are introduced due to the multiscale nature of such media [42,43,45,48,60]. In other words, we can use this imperfection (i.e. microporosity) to significantly improve sound absorption in 3D printed materials. This has been illustrated with a comprehensive example that can serve as benchmark for multiscale modelling as well as additive manufacturing of double- and single-porosity sound absorbers. In this example the sound absorption curves measured in the impedance tube from samples of engineered materials additively manufactured by two different technologies are compared with the results predicted from multiscale analyses, and also confronted with imperfections identified by microscopic examinations. The main conclusions and observations from this study are summarised below.

High-quality 3D printers in SLA technology can, with high precision, produce materials with a designed periodic network of pores characterised by sizes and shapes similar to those tested in this work. However, these characteristic sizes are at least several times larger that the ones found in conventional acoustic foams and this cannot be improved when using inexpensive devices, i.e. with typical 3D-printing resolutions used nowadays in SLA and other AM technologies. Nevertheless, the measured sound absorption of such periodic materials 3D-printed from photopolymer resins can be accurately predicted from the geometric representations of their periodic pore networks provided that the crucial dimensions of pores and especially channels connecting them are updated to their actual values. Often the necessary corrections can be anticipated based on the known resolution of the 3D printer and the acquired user experience, so they can be taken into account during the design process.

Geometry adjustments are usually slightly larger and more difficult to make or account for in other additive manufacturing technologies where also larger discrepancies are to be expected due to additional imperfections like surface roughness, etc. As already reported, e.g. in [17,16], and also confirmed in this work in particular by the results obtained from impregnated CJP samples, small surface imperfections often increase the sound absorption, usually between the peaks and without significantly changing the overall

nature of the absorption curves. However, when the imperfections become significant, it is obvious that the overall absorption will change drastically and will be far from predictions based on periodic geometries which are too idealised and inconsistent with reality. In general, some increase in sound absorption is often gained, but in more drastic cases these imperfections may reduce absorption.

An important imperfection that may appear in the additive manufacturing process is the microporosity of the 3D-printed skeleton. This can happen especially when 3D printing from powdered materials [38–40], i.e. when using laser sintering (of polymer powders) or laser melting (of metal powders), or binder jet 3D printing technologies [3,4] (like CJP used in this work). As demonstrated in this study, the adequate open microporosity of the 3D-printed skeleton of the acoustic material leads to an advantageous double porosity that strongly affects the propagation and absorption of acoustic waves in such media. When, in addition, the material design accounts for a permeability of the main pore network which is highly contrasted with that of the microporous skeleton, the pressure diffusion phenomena emerges and typically shifts the absorption peaks to lower frequencies and greatly increases the absorption between them. Since the shapes and proportions of the main pore network and (at the same time) microporous skeleton can be designed, this phenomenon, as well as the visco-thermal effects in the main pores, can be tuned and optimised in order to obtain the best required properties of the acoustic material designed and 3D-printed in this way. It has been shown how such double-porosity materials, and in particular the pressure diffusion effect, can be designed and accurately modelled using a rigorous multiscale approach. The predictions obtained in this way agree very well with the experimental results and it seems that the strong sound absorption effects due to pressure diffusion dominate over those related to shape and surface imperfections and uncertainties.

In summary, this work demonstrates that the possibility of additive manufacturing of double-porosity materials with designed main pore networks adequately contrasted with micropores opens up new perspectives for the use of low-cost 3D-printing devices for the production of innovative, carefully designed acoustic materials. It seems that due to the still insufficient resolution available in these devices, single-porosity solutions can be proposed as efficient mainly around specified frequencies. However, when double-porosity designs can be realised thanks to the deliberately introduced microporosity of the skeleton, the absorption between the peaks can be greatly increased due to the additional dissipation effect of pressure diffusion, providing broadband sound absorption in the medium frequency range (typical of conventional porous foams), while the specially engineered, e.g. extremely tortuous or labyrinthine [68], main pore networks can target high acoustic performance at very low frequency. It is clear that such solutions should be the subject of further research, including also additive manufacturing of optimised acoustic composites (or at least some of their components) with two [69,70] or even multiple scales [71] of porosity.

CRediT authorship contribution statement

Tomasz G. Zieliński: Conceptualization, Investigation, Formal analysis, Methodology, Resources, Software, Visualization, Writing – original draft, Writing – review & editing. **Nicolas Dauchez:** Conceptualization, Investigation, Resources, Supervision, Writing – review & editing. **Thomas Boutin:** Investigation. **Mikel Leturia:** Investigation. **Alexandre Wilkinson:** Investigation. **Fabien Chevillotte:** Investigation, Formal analysis, Validation, Writing – review & editing. **François-Xavier Bécot:** Investigation, Writing – review & editing. **Rodolfo Venegas:** Investigation, Validation, Writing – review & editing.

Declaration of Competing Interest

The authors declare that they have no known competing financial interests or personal relationships that could have appeared to influence the work reported in this paper.

Acknowledgements

T. G. Zieliński acknowledges the financial support from the project “Sound-absorbing composites: coupled acoustic energy dissipation mechanisms, multiscale modelling and prototyping”, financed under Grant Agreement No. 2021/41/B/ST8/04492 by the National Science Centre (NCN), Poland. R. Venegas acknowledges support from the Chilean National Agency for Research and Development (ANID) through FONDECYT Grant No. 1211310.

Appendix A. Scaling function

Frequency-dependent dynamic permeabilities related to the visco-inertial effects, as well as thermal and pressure diffusions can be determined using the following scaling function

$$\mathcal{X}_\omega(\mathcal{X}_0,\omega_c,\mathcal{M},\mathcal{P})=\mathcal{X}_0\left(\frac{\mathrm{i}\omega}{\omega_c}+1-\mathcal{P}+\sqrt{\mathcal{P}^2+\frac{\mathcal{M}}{2}\frac{\mathrm{i}\omega}{\omega_c}}\right)^{-1} \tag{A.1}$$

where $\mathcal{X}_0$ is the corresponding static value (i.e. for $\omega=0$), while $\omega_c,\mathcal{M}$, and $\mathcal{P}$ are the characteristic frequency, shape factor, and low-frequency correction coefficient, respectively. This scaling function is usually referred to as the Johnson-Champoux-Allard-Lafarge-Pride (JCALP) model [72,73,51,52,74,61]. If the low-frequency correction is neglected, i.e. for $\mathcal{P}=1$, the function $\mathcal{X}_\omega(\mathcal{X}_0,\omega_c,\mathcal{M},1)$ is called the Johnson-Champoux-Allard-Lafarge (JCAL) model. Due to the problem with the determination of static thermal permeability (in particular by direct measurement), the shape factor for thermal effects is often assumed to be 1, which in many cases is acceptable. This early original version of the model (i.e. when $\mathcal{P}=\mathcal{P}_\mathrm{v}=\mathcal{P}_\mathrm{t}=1$ and the dynamic thermal permeability is determined for $\mathcal{M}=\mathcal{M}_\mathrm{t}=1$) is referred to as the Johnson-Champoux-Allard (JCA) model.

Appendix B. Calculations at lower scales

B.1. Visco-inertial effects

The acoustically induced fluid flow can be assumed incompressible in a sufficiently small REV Ω_p (in the considered scale, e.g. the mesoscopic scale adopted here), so that the visco-inertial and thermal effects can be decoupled. The visco-inertial effects are associated with the oscillatory viscous incompressible flow through the periodic pore network Ω_pf (see Fig. 1) with open porosity ϕ_p, driven by the macroscopic (i.e. constant in the entire Ω_pf) pressure gradient (harmonically changing in time) acting in the propagation direction specified by the unit vector $\mathbf{e}$, with no-slip boundary conditions of the skeleton walls Γ_p bounding the pore network (see Fig. 1). The equations governing the oscillatory flow have to be solved for each computational frequency ω; they can be scaled to the following form

$$\frac{\mathrm{i}\omega}{\nu}\tilde{\mathbf{k}}-\nabla^2\tilde{\mathbf{k}}+\nabla\tilde{q}=\mathbf{e}\quad\text{and}\quad\nabla\cdot\tilde{\mathbf{k}}=0\quad\text{in }\Omega_\mathrm{pf}, \tag{B.1}$$

$$\tilde{\mathbf{k}}=\mathbf{0}\quad\text{on }\Gamma_\mathrm{p}, \tag{B.2}$$

where $\tilde{\mathbf{k}}(\omega)$ is the Ω_p-periodic velocity field scaled to the permeability unit (i.e. metre squared) and $\tilde{q}(\omega)$ is the Ω_p-periodic local pressure field scaled to the unit of length (i.e. metre). After the scaled flow problem has been solved, the dynamic viscous permeability (or rather its projection on the propagation direction $\mathbf{e}$) is calculated as

$$\mathcal{K}_\mathrm{p}(\omega) = \phi_\mathrm{p}\langle\tilde{\mathbf{k}}(\omega)\cdot\mathbf{e}\rangle_{\Omega_\mathrm{pf}}, \tag{B.3}$$

where $\langle\cdot\rangle_{\Omega_\mathrm{pf}} \equiv \int_{\Omega_\mathrm{pf}}(\cdot)\,\mathrm{d}\Omega / \int_{\Omega_\mathrm{pf}}\mathrm{d}\Omega$ is the spatial averaging operator. Usually, $\mathcal{K}_\mathrm{p}(\omega)$ can be accurately approximated using the scaling function (A.1) with $\mathcal{X}_0 = \mathcal{K}_{0\mathrm{p}}$, and $\omega_\mathrm{c} = \omega_{\mathrm{vp}}, \mathcal{M} = \mathcal{M}_{\mathrm{vp}}, \mathcal{P} = \mathcal{P}_{\mathrm{vp}}$, determined using formulae (4), where the required parameters $\mathcal{K}_{0\mathrm{p}}, \alpha_{0\mathrm{vp}}, \alpha_{\infty\mathrm{p}}$, and Λ_{vp} are found from the solutions of two problems related to the low- and high-frequency regimes as detailed below.

At low frequencies, the inertial effects can be neglected. In particular, for $\omega = 0$ the scaled oscillatory viscous flow (B.1)–(B.2) becomes Stokes' flow, which is governed by

$$-\nabla^2\mathbf{k} + \nabla q = \mathbf{e} \quad\text{and}\quad \nabla\cdot\mathbf{k} = 0 \quad \text{in } \Omega_\mathrm{pf}, \tag{B.4}$$

$$\mathbf{k} = \mathbf{0} \quad \text{on } \Gamma_\mathrm{p}, \tag{B.5}$$

where the unknown (static) fields, $\mathbf{k} \equiv \tilde{\mathbf{k}}(0)$ and $q \equiv \tilde{q}(0)$, are real-valued and Ω_p-periodic. The static viscous permeability and tortuosity are determined from the solution of this problem as

$$\mathcal{K}_{0\mathrm{p}} = \phi_\mathrm{p}\langle\mathbf{k}\cdot\mathbf{e}\rangle_{\Omega_\mathrm{pf}}, \qquad \alpha_{0\mathrm{vp}} = \frac{\langle\mathbf{k}\cdot\mathbf{k}\rangle_{\Omega_\mathrm{pf}}}{\langle\mathbf{k}\rangle_{\Omega_\mathrm{pf}}\cdot\langle\mathbf{k}\rangle_{\Omega_\mathrm{pf}}}. \tag{B.6}$$

In the high-frequency regime, i.e. for $\omega \to \infty$, the viscous effects can be neglected. It has been demonstrated [75,76] that the incompressible *inviscid* flow through a porous medium formally coincides with the problem of the electrical conductivity of the porous medium consisting of an electrically insulating skeleton and a pore network saturated with a conductive fluid, namely

$$\mathbf{E} + \nabla u = \mathbf{e} \quad\text{and}\quad \nabla\cdot\mathbf{E} = 0 \quad \text{in } \Omega_\mathrm{pf}, \tag{B.7}$$

$$\mathbf{E}\cdot\mathbf{n} = 0 \quad \text{on } \Gamma_\mathrm{p}, \tag{B.8}$$

where $\mathbf{E}$ and u are the Ω_p-periodic electric field and the corresponding electric potential, respectively (both defined in the domain Ω_pf of the conductive fluid), $\mathbf{n}$ is the unit vector normal to the insulating boundary Γ_p (pointing outside the Ω_pf domain), and $\mathbf{e}$ is the externally-applied, macroscopic (i.e. constant in the entire Ω_pf) electric field. Note that the problem can be scaled, so that $\mathbf{E}$ and $\mathbf{e}$ are dimensionless ($\mathbf{e}$ is the unit vector specifying the direction of the external field collinear with the propagation direction) and the potential u has the unit of length (i.e. metre). This electric conductivity (or perfect fluid flow) problem (B.7)–(B.8) reduces to the Laplace's problem for the potential u, namely

$$\nabla^2 u = 0 \quad \text{in } \Omega_\mathrm{pf}, \tag{B.9}$$

$$\nabla u\cdot\mathbf{n} = \mathbf{e}\cdot\mathbf{n} \quad \text{on } \Gamma_\mathrm{p}. \tag{B.10}$$

After the solution u has been found, and then also the vector field $\mathbf{E} = \mathbf{e} - \nabla u$, the tortuosity and viscous characteristic length are calculated as

$$\alpha_{\infty\mathrm{p}} = \frac{\langle\mathbf{E}\cdot\mathbf{E}\rangle_{\Omega_\mathrm{pf}}}{\langle\mathbf{E}\rangle_{\Omega_\mathrm{pf}}\cdot\langle\mathbf{E}\rangle_{\Omega_\mathrm{pf}}}, \qquad \Lambda_{\mathrm{vp}} = 2\frac{\int_{\Omega_\mathrm{pf}}\mathbf{E}\cdot\mathbf{E}\,\mathrm{d}\Omega}{\int_{\Gamma_\mathrm{p}}\mathbf{E}\cdot\mathbf{E}\,\mathrm{d}\Gamma}. \tag{B.11}$$

B.2. Thermal effects and pressure diffusion

Consider the REV Ω_p (see Fig. 1) of a periodic medium consisting of the pore network Ω_pf with an open (meso-scale) porosity ϕ_p and the (microporous) skeleton Ω_ps occupying a fraction $\phi_\mathrm{d} = 1 - \phi_\mathrm{p}$ of the Ω_p volume, with the interface Γ_p between both subdomains.

Pressure fluctuations due to the fluid-borne acoustic waves propagating in the medium cause temperature fluctuations inside the fluid-saturated pore network. The resulting heat transfer is quickly absorbed at Γ_p by the solid skeleton due to its much higher volumetric heat capacity and thermal conductivity than that of the fluid, which means that isothermal conditions are kept on the boundary Γ_p. The fluid in the pore network is characterised by its thermal diffusivity ν_t, and the local phenomenon is thermal diffusion caused by oscillatory volumetric heat source (its power is uniform in the entire Ω_pf domain) due to harmonic oscillations of the macroscopic acoustic pressure. The process equations can be scaled, so that the volumetric heat source power is a dimensionless unit and the *scaled* complex amplitude of temperature fluctuations $\tilde{\theta}$ (defined in Ω_pf) has the unit of permeability (i.e. metre squared). The dynamic thermal permeability Θ_p, which determines the effective compressibility $\mathcal{C}_\mathrm{p}$ according to the formula (5), is calculated as the average of the scalar field $\tilde{\theta}$ over the entire REV, which means integration over the Ω_pf domain (i.e. where this field is defined) and division by the volume of the representative cell, see Eq. (B.14) below.

In the case of double-porosity media, their effective compressibility $\mathcal{C}_\mathrm{db}$ depends on $\mathcal{C}_\mathrm{p}$, but also on the effective compressibility $\mathcal{C}_\mathrm{m}$ determined for the microporous material of the skeleton, e.g. from the corresponding periodic REV Ω_m (see Fig. 1). For materials with low permeability contrast between their mesoporous and microporous networks, $\mathcal{C}_\mathrm{db}$ can be immediately calculated using formula (15), but when the permeability contrast is high enough, the pressure diffusion inside the microporous skeleton leads to additional energy dissipation and thus strongly affects $\mathcal{C}_\mathrm{db}$, which must be calculated using formula (12) containing the function $\mathcal{F}_\mathrm{d}$ related to pressure diffusion. The microporous material of the skeleton (saturated with a fluid of dynamic viscosity η) is characterised by the dynamic and static pressure diffusivities, $\mathcal{D}_\mathrm{m}(\omega)$ and $\mathcal{D}_{0\mathrm{m}} \equiv \mathcal{D}_\mathrm{m}(0)$, respectively, defined according to the formulae (8). The function $\mathcal{F}_\mathrm{d}(\omega)$ depends on $\mathcal{D}_\mathrm{m}(\omega)$ and also on a dynamic pressure diffusion $\mathcal{B}_\mathrm{d}(\omega)$, according to the formula (14). The dynamic function $\mathcal{B}_\mathrm{d}$ is very similar to the dynamic thermal permeability Θ_p. It is calculated as the average of a scalar field $\tilde{\theta}$ over the entire REV, see Eq. (B.15) below, although this time $\tilde{\theta}$ is defined in Ω_ps as the complex amplitude of local pressure fluctuations in the micropores around the constant pressure in the pores, whereby this difference is suitably scaled to the permeability unit (i.e. metre squared). Note that for the sake of brevity of the formulae presented below, we use the same symbol $\tilde{\theta}$ for the field associated with pressure diffusion as for the field related to thermal diffusion, although they are physically different fields defined in different domains.

As mentioned above, the phenomena related to thermal diffusion in the pores and pressure diffusion in the micropores are formally described by the same kind of boundary value problem, although in different subdomains, i.e. in Ω_pf or Ω_ps, respectively. Thus, for each computational frequency ω, the scaled equations of the oscillatory thermal flow or pressure diffusion can be expressed as follows

$$\frac{\mathrm{i}\omega}{\mathcal{D}}\tilde{\theta} - \nabla^2\tilde{\theta} = 1 \quad \text{in } \Omega_\star \tag{B.12}$$

$$\tilde{\theta} = 0 \quad \text{on } \Gamma_\mathrm{p}, \tag{B.13}$$

where $\mathcal{D} = \nu_\mathrm{t}$ and $\Omega_\star = \Omega_\mathrm{pf}$ in the case of thermal diffusion, whereas $\mathcal{D} = \mathcal{D}_\mathrm{m}(\omega) \approx \mathcal{D}_{0\mathrm{m}}$ and $\Omega_\star = \Omega_\mathrm{ps}$ in the case of pressure diffusion. In addition, the unknown scalar field $\tilde{\theta}(\omega)$, being Ω_p-periodic, must satisfy periodic boundary conditions at the respective lateral boundaries of the periodic representative cell

Ω_p. Note that even for double-porosity media, the thermal diffusion problem (defined in the main pore network) is solved in Ω_{pf}, assuming the entirely isothermal boundary Γ_p (thermal effects are neglected in the micropores). Similarly, the pressure diffusion problem is solved independently in the Ω_{ps} domain. After the solution has been found for the problem defined in the fluid domain Ω_{pf}, the dynamic thermal permeability is calculated as the average over the entire periodic cell, namely

$$\Theta_p(\omega) = \phi_p \langle \tilde{\theta}(\omega) \rangle_{\Omega_{pf}}. \tag{B.14}$$

In the case when the problem is solved in the skeleton domain Ω_{ps}, a similar dynamic function is computed for pressure diffusion as

$$\mathcal{B}_d(\omega) = \phi_d \langle \tilde{\theta}(\omega) \rangle_{\Omega_{ps}}. \tag{B.15}$$

In practice, both $\Theta_p(\omega)$ and $\mathcal{B}_d(\omega)$ can often be accurately approximated using the scaling function (A.1). Then, in the case of thermal diffusion: $\mathcal{X}_0 = \Theta_{0p}$, while $\omega_c = \omega_{tp}, \mathcal{M} = \mathcal{M}_{tp}$, and $\mathcal{P} = \mathcal{P}_{tp}$ are determined using formulae (6) together with the 'static' thermal parameters Θ_{0p} and α_{0tp}, computed from the 'static' field $\theta \equiv \tilde{\theta}(0)$, and the characteristic length Λ_{tp}, defined as follows

$$\Theta_{0p} = \phi_p \langle \theta \rangle_{\Omega_{pf}}, \qquad \alpha_{0tp} = \frac{\langle \theta^2 \rangle_{\Omega_{pf}}}{\langle \theta \rangle^2_{\Omega_{pf}}}, \qquad \Lambda_{tp} = 2 \frac{\int_{\Omega_{pf}} \mathrm{d}\Omega}{\int_{\Gamma_p} \mathrm{d}\Gamma}. \tag{B.16}$$

Similarly, in the case of pressure diffusion: $\mathcal{X}_0 = \mathcal{B}_{0d}$, while $\omega_c = \omega_d, \mathcal{M} = \mathcal{M}_d$, and $\mathcal{P} = \mathcal{P}_d$ are determined using formulae (13) and the following 'static' parameters and characteristic length

$$\mathcal{B}_{0d} = \phi_d \langle \theta \rangle_{\Omega_{ps}}, \qquad \alpha_{0d} = \frac{\langle \theta^2 \rangle_{\Omega_{ps}}}{\langle \theta \rangle^2_{\Omega_{ps}}}, \qquad \Lambda_d = 2 \frac{\int_{\Omega_{ps}} \mathrm{d}\Omega}{\int_{\Gamma_p} \mathrm{d}\Gamma}. \tag{B.17}$$

Note that $\Lambda_d/\phi_d = \Lambda_{tp}/\phi_p$. In both cases, the 'static' parameters are found from the solution θ of the corresponding Poisson's problem

$$-\nabla^2 \theta = 1 \quad \text{in} \begin{cases} \Omega_{pf} & \text{– in the case of thermal diffusion,} \\ \Omega_{ps} & \text{– in the case of pressure diffusion,} \end{cases} \tag{B.18}$$

$$\theta = 0 \quad \text{on } \Gamma_p, \tag{B.19}$$

obtained by setting $\omega = 0$ in Eqs. (B.12) and (B.13).

Appendix C. Characterisation of microporous material and 3D-printed single-porosity samples

C.1. Properties of microporous material

The airflow resistivity of the microporous material was measured using a *Mecanum Static Airflow Resistivity Meter*, Model *SIG 2011*, according to ISO standard [77]. The measurements were performed on four identical microporous discs (100 mm in diameter and 14.9 mm thick) manufactured for the purpose. The discs were 3D printed in CJP technology using the same device, process parameters, material (i.e. gypsum-based powder) and binder as used for the CJP samples studied in Section 3. The edges around each measured disc-shaped sample were sealed with vacuum grease to ensure no air leakage gaps. The airflow resistivity was measured for one disc at a time. An additional measurement was performed on one of the discs to obtain more data for statistical analysis, and to account for changing experimental conditions throughout the measurement process. Table C.1 presents the static airflow resistivity measured for the discs, as well as the average value for all measurements and standard deviation. Based on these very consistent results, the static, viscous permeability $\mathcal{K}_{0m}$ of the microporous material (present in all non-impregnated CJP samples) can be assessed with high reliability as $\mathcal{K}_{0m} = \eta/\sigma_{0m} \approx 5.7 \cdot 10^{-13}\,\mathrm{m}^2$ (here: $\sigma_{0m} = 32.24\,\mathrm{MPa{\cdot}s/m^2}$ is the average value from Table C.1, and $\eta = 1.847 \cdot 10^{-5}\,\mathrm{Pa{\cdot}s}$ is the dynamic air viscosity determined for the ambient conditions occurring during the measurements of airflow resistivity, i.e. at 25°C). This value ensures the appropriate high permeability contrast when compared with the permeabilities $\mathcal{K}_{0p}$ (of order $10^{-8}\,\mathrm{m}^2$) of the designed main pore networks. The disc samples were also used for the microporosity measurements discussed below.

The open porosity was measured with a *Mecanum Open Porosity & Density Meter*, Model *PHI 2011* [78], for: (i) four non-impregnated, i.e. microporous CJP discs – the result was 42.6%; (ii) four non-impregnated, i.e. double-porosity CJP samples – the result was 73%; (iii) four impregnated, i.e. single-porosity CJP samples – the result was 52.5%. The result obtained for the discs is obviously the microporosity $\phi_m = 0.426$ of the material made in the CJP technology using the indicated 3D printer, powder and binder, while the result measured for the non-impregnated samples is the average total open porosity $\phi_t = 0.73$ of these double-porosity structures. The impregnation process closes the micropores. Therefore, the result measured for the impregnated samples is the average porosity $\phi_p = 0.525$ of their main pore networks. Note that the porosity relationship holds, i.e. $\phi_t \simeq \phi_p + (1 - \phi_p)\phi_m$.

To relate the microporosity to the average grain size of the gypsum powder used for 3D printing, the particle size distribution of the dry powder was measured with a *Mastersizer 3000* laser granulometer manufactured by *Malvern Instruments*. As the particles may be initially agglomerated, the dry powder disperser *Aero S* was used to disperse the particles without breaking them. The dispersion pressure was set to 3 bars. Fig. C.1 shows the measured particle size distribution and demonstrates that the grain size range is large, namely the smallest particles have sizes (defined as diameters of the equivalent spheres) less than 1 µm, while the largest particle sizes are around 140 µm. The volumetric average is 41 µm, however, when studying viscous flows through a packed bed of particles, more appropriate is the so-called Sauter mean diameter, a.k.a. the volume–surface mean diameter, defined as the diameter of a sphere that has the same volume-to-surface area ratio as the entire set of particles [79,80]. It is 17 µm in the case of dry gypsum powder. On the other hand, it should not be forgotten that in the 3D-printed material, the grains may be agglomerated and are coated with a binder, so that the effective average diameter of grains in CJP samples should be slightly larger. When this value is set to 20 µm (i.e. the effective grain radius is $R_g = 10\,\mu\mathrm{m}$), then, for such a simplified granular medium represented by a single grain diameter and (measured) open porosity $\phi_m = 0.426$, the viscous permeability calculated from the first formula in Eqs. (D.1) corresponds to the measured value $\mathcal{K}_{0m} \approx 5.7 \cdot 10^{-13}\,\mathrm{m}^2$.

C.2. Acoustic characterisation of the macro-parameters of 3D-printed samples with single porosity

Macro-parameters associated with the porous networks of the single-porosity samples can be characterised by acoustic measurements. The procedure can be briefly explained as follows. A porous

Table C.1
Measurements of static airflow resistivity.

	σ_{0m} (Pa·s/m^2)	
Measurement 1	32320283	
Measurement 2	32509749	
Measurement 3	31780556	
Measurement 4	32094197	
Measurement 5	32481866	
Average (std. dev.)	32237330	(3041146)

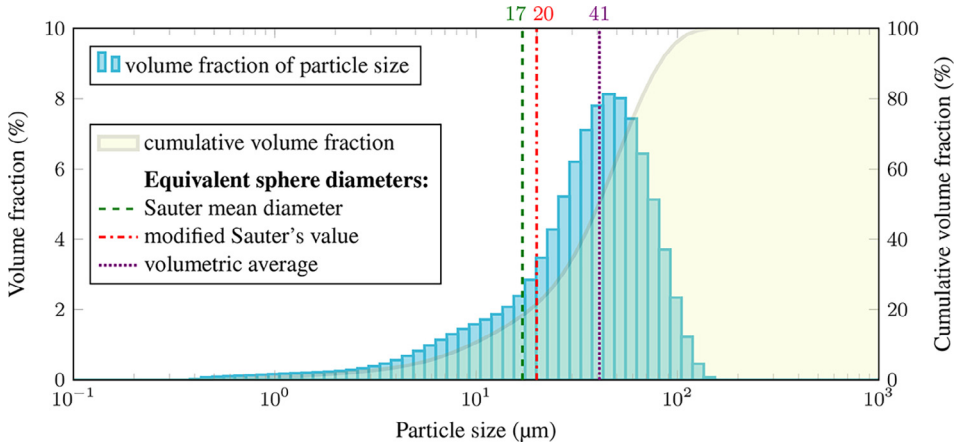

Fig. C.1. Particle size distribution of the gypsum powder used for 3D printing.

sample of known thickness is tested twice in an impedance tube (equipped with two microphones), so that during successive measurements of the surface acoustic impedance, the same sample is backed by an air gap of two different thicknesses. Based on the two measured acoustic impedances and the a priori known impedances of both air gaps, one can determine the effective characteristic impedance $Z_p(\omega)$ and complex wave number $k_p(\omega)$ (or propagation constant) for the porous material, as shown by Utsuno et al. [81]. Alternatively, the three-microphone technique can be used [82,83]. The advantage is that no air gaps behind the tested sample are required in these measurements. Once Z_p and k_p have been determined, the effective density $\varrho_p(\omega)$ and the effective compressibility $\mathcal{C}_p(\omega)$, or better its reciprocal $1/\mathcal{C}_p$, i.e. the effective bulk modulus, are calculated as $\varrho_p = Z_p k_p/\omega$ and $1/\mathcal{C}_p = \omega Z_p/k_p$, respectively. As demonstrated by Panneton and Olny [84,85] and Jaouen et al. [86], these two directly measured effective properties can be used to determine the macro-parameters of the porous material required by the JCA and JCAL models, see Appendix A along with the formulae (4) and (6). For example, the porosity can be estimated from low- and high-frequency asymptotes of the real part of the effective bulk modulus [87], viz. $\phi_p = P_0/\lim_{\omega\to 0}\mathrm{Re}(1/\mathcal{C}_p) = \gamma P_0/\lim_{\omega\to\infty}\mathrm{Re}(1/\mathcal{C}_p)$, while the static airflow resistivity from the imaginary part of the effective density, viz. $\sigma_{0p} = \lim_{\omega\to 0}(-\omega\mathrm{Im}\varrho_p)$. Recall that the latter is directly related to the (fluid-independent) static viscous permeability, viz. $\mathcal{K}_{0p} = \eta/\sigma_{0p}$. This approach is known as analytic inversion or indirect method. Another possibility is purely inverse methods that involve curve fitting procedures, see e.g. [88–90]. In general, these methods are easier to implement but can lead to inconsistent or non-physical output parameter sets. In this study, the single-porosity samples were characterised using the indirect method (with the three-microphone technique) in conjunction with the Bayesian minimization procedure to take advantage of both approaches. This enabled to constrain the curve fitting procedure to physical parameters and their associated uncertainties while refining the statistical analysis. Finally, to ensure the accuracy of the characterisation, the airflow resistivity and porosity of samples were measured directly according to Refs. [77,78], respectively.

Table C.2 shows the macro-parameters characterised by acoustic measurements of four impregnated CJP samples and four SLA samples. Additional SLA specimens were produced and tested to enrich the statistics. The averaged values are presented for the samples of the same cell size and their standard deviations are given in parentheses. For convenience, the corresponding results of numerical analyses of visco-inertial and thermal effects in the respective REV have been copied from Table 3 for comparison. Relevant results calculated for the original (i.e. not updated) REV of CAD models used to 3D print samples are also included. To analyse the uncertainties in the characterisation of parameters and the manufacturing process, Table C.3 allows for a collective comparison of the results obtained by experimental characterisation and numerical simulations. Here, the values of a parameter characterised from all single-porosity samples of the same cell size ℓ_p served as statistical data to determine the appropriate mean value (with the standard deviation given in parentheses). The same procedure was applied to the results of numerical simulations carried out on the REVs of the same size ℓ_p. For the convenience of comparison, even the numerically obtained mean values of airflow resistivity σ_{0p} and their standard deviations were rounded up in this

Table C.2
Macro-parameters for single-porosity samples: characterisation results from acoustic measurements compared to numerical calculations based on REV.

Method Method	Type Type	ℓ_p mm	ϕ_p %	σ_{0p} Pa·s/m^2	Θ_{0p} 10^{-10}m^2	Λ_{vp} μm	Λ_{tp} μm	$\alpha_{\infty p}$ –
Characterisation	**SLA**	3	46 (3)	1300 (100)	199 (22)	460 (51)	1028 (542)	1.85 (0.03)
from samples	impreg.**CJP**	3	49 (1)	1300 (100)	187 (24)	322 (19)	592 (116)	1.85 (0.07)
REV-based	CAD	3	44.1	1255	609	678	1097	1.78
numerical	**SLA**	3	41.7	1678	538	623	1038	1.91
calculations	**CJP**	3	49.6	1357	772	631	1149	1.92
Characterisation	**SLA**	4	46 (2)	700 (100)	323 (83)	560 (106)	927 (246)	1.82 (0.07)
from samples	impreg. **CJP**	4	51 (1)	700 (100)	267 (33)	384 (32)	768 (292)	1.88 (0.06)
REV-based	CAD	4	44.1	706	1082	904	1462	1.78
numerical	**SLA**	4	42.3	879	986	850	1403	1.87
calculations	**CJP**	4	50.7	694	1440	862	1562	1.88

Table C.3
Collective comparison of the characterisation and simulation results.

Method Method	ℓ_p mm	ϕ_p %	σ_{0p} Pa·s/m^2	Θ_{0p} 10^{-10}m^2	Λ_{vp} μm	Λ_{tp} μm	$\alpha_{\infty p}$ –
Characterisations	3	46 (3)	1300 (100)	197 (23)	425 (77)	919 (503)	1.85 (0.03)
REV calculations	3	45 (4)	1500 (200)	640 (120)	644 (30)	1095 (56)	1.87 (0.08)
Characterisations	4	47 (3)	700 (100)	314 (79)	516 (121)	885 (259)	1.84 (0.07)
REV calculations	4	46 (5)	800 (100)	1169 (293)	872 (28)	1476 (80)	1.84 (0.06)

table to the precision available in direct measurements of this parameter.

In general, the identified values of porosity ϕ_p and tortuosity $\alpha_{\infty p}$ agree with their numerically calculated counterparts. Also, the acoustically determined values of the static airflow resistivity σ_{0p} correspond very well with the results calculated from the numerically determined static viscous permeability $\mathcal{K}_{0p}$, especially in the case of CJP samples and in the collective comparison, see Table C.3. On the other hand, the characteristic lengths have not been correctly identified: they are significantly smaller than their numerically calculated counterparts; the latter are as expected, i.e. Λ_{vp} is slightly larger than the radius of the cylindrical channels connecting the pores and Λ_{tp} is greater than $\frac{2}{3}$ of the pore radius. It is known that the correct identification of the characteristic lengths, especially Λ_{vp}, is difficult and is usually achieved with little accuracy [84]. Nevertheless, a comparison of the cumulative values of the characteristic lengths given in Table C.3 shows moderate agreement when their standard deviations are also taken into account.

Appendix D. Estimation of macro-parameters for granular media

Let ϕ_m be the porosity of a granular medium and R_g the (average) grain radius. The macro-parameters for such media can be estimated using the following formulae [91,92]:

$$\begin{aligned} &\mathcal{K}_{0m} = \tfrac{2-3\beta+3\beta^5-2\beta^6}{9\beta^3+6\beta^8}R_g^2, \qquad \Theta_{0m} = \tfrac{5-9\beta+5\beta^3-\beta^6}{15\beta^3}R_g^2, \\ &\Lambda_{tm} = \tfrac{2\phi_m}{3-3\phi_m}R_g, \qquad \Lambda_{vm} = \tfrac{3-\phi_m}{3}\Lambda_{tm}, \qquad \alpha_{\infty m} = \tfrac{3-\phi_m}{2}, \end{aligned} \tag{D.1}$$

where $\beta = (1-\phi_m)^{1/3}$. The static tortuosities are such that low-frequency corrections are neglected, i.e. $\mathcal{P}_{vm} = \mathcal{P}_{tm} = 1$. The corresponding dynamic viscous $\mathcal{K}_m(\omega)$ and thermal $\Theta_m(\omega)$ permeabilities can be determined using the scaling function (A.1) and the formulae (4) and (6), respectively, in which the subscript "p" is replaced by "m".

References

[1] Gibson I, Rosen D, Stucker B. Additive Manufacturing Technologies: 3D Printing, Rapid Prototyping, and Direct Digital Manufacturing. 2nd ed. New York: Springer; 2015. https://doi.org/10.1007/978-1-4939-2113-3.

[2] Ngo TD, Kashani A, Imbalzano G, Nguyen KT, Hui D. Additive manufacturing (3D printing): A review of materials, methods, applications and challenges. Compos Part B: Eng 2018;143:172–96. https://doi.org/10.1016/j.compositesb.2018.02.012.

[3] Dini F, Ghaffari SA, Jafar J, Hamidreza R, Marjan S. A review of binder jet process parameters; powder, binder, printing and sintering condition. Met Powder Rep 2020;75:95–100. https://doi.org/10.1016/j.mprp.2019.05.001.

[4] Mostafaei A, Elliott AM, Barnes JE, Li F, Tan W, Cramer CL, Nandwana P, Chmielus M. Binder jet 3D printing—Process parameters, materials, properties, modeling, and challenges. Prog Mater Sci 2021;119:100707. https://doi.org/10.1016/j.pmatsci.2020.100707.

[5] Melchels FP, Feijen J, Grijpma DW. A review on stereolithography and its applications in biomedical engineering. Biomaterials 2010;31:6121–30. https://doi.org/10.1016/j.biomaterials.2010.04.050.

[6] Zhang F, Zhu L, Li Z, Wang S, Shi J, Tang W, Li N, Yang J. The recent development of vat photopolymerization: A review. Addit Manuf 2021;48:102423. https://doi.org/10.1016/j.addma.2021.102423.

[7] Setaki F, Tenpierik M, Turrin M, van Timmeren A. Acoustic absorbers by additive manufacturing. Build Environ 2014;72:188–200. https://doi.org/10.1016/j.buildenv.2013.10.010.

[8] Liu Z, Zhan J, Fard M, Davy J. Acoustic properties of a porous polycarbonate material produced by additive manufacturing. Mater Lett 2016;181:296–9. https://doi.org/10.1016/j.matlet.2016.06.045.

[9] Liu Z, Zhan J, Fard M, Davy J. Acoustic properties of multilayer sound absorbers with a 3D printed micro-perforated panel. Appl Acoust 2017;121:25–32. https://doi.org/10.1016/j.apacoust.2017.01.032.

[10] Carbajo J, Ghaffari Mosanenzadeh S, Kim S, Fang NX. Sound absorption of acoustic resonators with oblique perforations. Appl Phys Lett 2020;116:054101. https://doi.org/10.1063/1.5132886.

[11] Carbajo J, Ghaffari Mosanenzadeh S, Kim S, Fang N. Multi-layer perforated panel absorbers with oblique perforations. Appl Acoust 2020;169:107496. https://doi.org/10.1016/j.apacoust.2020.107496.

[12] Carbajo J, Molina-Jordá J, Maiorano L, Fang N. Sound absorption of macro-perforated additively manufactured media. Appl Acoust 2021;182:108204. https://doi.org/10.1016/j.apacoust.2021.108204.

[13] Zieliński TG, Chevillotte F, Deckers E. Sound absorption of plates with micro-slits backed with air cavities: Analytical estimations, numerical calculations and experimental validations. Appl Acoust 2019;146:261–79. https://doi.org/10.1016/j.apacoust.2018.11.026.

[14] Zieliński TG. Pore-size effects in sound absorbing foams with periodic microstructure: modelling and experimental verification using 3D printed specimens. In: Sas P, Moens D, van de Walle A, editors. Proceedings of ISMA2016 International Conference on Noise and Vibration Engineering and USD2016 International Conference on Uncertainty in Structural Dynamics. p. 95–104.

[15] Zieliński TG, Opiela KC, Pawłowski P, Dauchez N, Boutin T, Kennedy J, Trimble D, Rice H. Differences in sound absorption of samples with periodic porosity produced using various Additive Manufacturing Technologies. In: Ochmann M, Vorländer M, Fels J, editors. Proceedings of the 23rd International Congress on Acoustics integrating 4th EAA Euroregio. p. 4505–12. https://doi.org/10.18154/RWTH-CONV-239456.

[16] Kennedy J, Flanagan L, Dowling L, Bennett GJ, Rice H, Trimble D. The influence of additive manufacturing processes on the performance of a periodic acoustic metamaterial. Int J Polym Sci 2019;2019:7029143. https://doi.org/10.1155/2019/7029143.

[17] Zieliński TG, Opiela KC, Pawłowski P, Dauchez N, Boutin T, Kennedy J, Trimble D, Rice H, Van Damme B, Hannema G, Wróbel R, Kim S, Ghaffari Mosanenzadeh S, Fang NX, Yang J, Briere de La Hosseraye B, Hornikx MC, Salze E, Galland M-A, Boonen R, Carvalho de Sousa A, Deckers E, Gaborit M, Groby J-P. Reproducibility of sound-absorbing periodic porous materials using additive manufacturing technologies: Round robin study. Addit Manuf 2020;36:101564. https://doi.org/10.1016/j.addma.2020.101564.

[18] McGee O, Jiang H, Qian F, Jiac Z, Wang L, Meng H, Chronopoulos D, Chen Y, Zuo L. 3D printed architected hollow sphere foams with low-frequency phononic band gaps. Addit Manuf 2019;30:100842. https://doi.org/10.1016/j.addma.2019.100842.

[19] Boulvert J, Cavalieri T, Costa-Baptista J, Schwan L, Romero-García V, Gabard G, Fotsing ER, Ross A, Mardjono J, Groby J-P. Optimally graded porous material for broadband perfect absorption of sound. J Appl Phys 2019;126:175101. https://doi.org/10.1063/1.5119715.

[20] Johnston W, Sharma B. Additive manufacturing of fibrous sound absorbers. Addit Manuf 2021;41:101984. https://doi.org/10.1016/j.addma.2021.101984.

[21] Boulvert J, Costa-Baptista J, Cavalieri T, Perna M, Fotsing ER, Romero-García V, Gabard G, Ross A, Mardjono J, Groby J-P. Acoustic modeling of micro-lattices obtained by additive manufacturing. Appl Acoust 2020;164:107244. https://doi.org/10.1016/j.apacoust.2020.107244.

[22] Li X, Yu X, Zhai W. Additively manufactured deformation-recoverable and broadband sound-absorbing microlattice inspired by the concept of traditional perforated panels. Adv Mater 2021;33:2104552. https://doi.org/10.1002/adma.202104552.

[23] Fotsing ER, Dubourg A, Ross A, Mardjono J. Acoustic properties of periodic micro-structures obtained by additive manufacturing. Appl Acoust 2019;148:322–31. https://doi.org/10.1016/j.apacoust.2018.12.030.

[24] Ring T, Langer S. Design, experimental and numerical characterization of 3D-printed porous absorbers. Materials 2019;12:3397. https://doi.org/10.3390/ma12203397.

[25] Opiela KC, Zieliński TG, Attenborough K. Manufacturing, modeling, and experimental verification of slitted sound absorbers. In: Desmet W, Pluymers B, Moens D, Vandemaele S, editors. Proceedings of ISMA2020

International Conference on Noise and Vibration Engineering and USD2020 International Conference on Uncertainty in Structural Dynamics. p. 409–20.
[26] Yang M, Chen S, Fu C, Sheng P. Optimal sound-absorbing structures. Mater Horizons 2017;4:673–80. https://doi.org/10.1039/C7MH00129K.
[27] Jiménez N, Romero-García V, Pagneux V, Groby J-P. Rainbow-trapping absorbers: Broadband, perfect and asymmetric sound absorption by subwavelength panels for transmission problems. Scientific Rep 2017;7:13595. https://doi.org/10.1038/s41598-017-13706-4.
[28] Rice HJ, Kennedy J, Göransson P, Dowling L, Trimble D. Design of a Kelvin cell acoustic metamaterial. J Sound Vib 2020;472:115167. https://doi.org/10.1016/j.jsv.2019.115167.
[29] Cavalieri T, Boulvert J, Romero-García V, Gabard G, Escouflaire M, Regnard J, Groby J-P. Rapid additive manufacturing of optimized anisotropic metaporous surfaces for broadband absorption. J Appl Phys 2021;129:115102. https://doi.org/10.1063/5.0042563.
[30] Opiela KC, Zieliński TG. Microstructural design, manufacturing and modelling of an adaptable porous composite sound absorber. Compos Part B: Eng 2020;187:107833. https://doi.org/10.1016/j.compositesb.2020.107833.
[31] Kim DH, Yoon GH. Active acoustic absorption device using additive manufacturing technique for normal incident wave. Appl Acoust 2021;178:108006. https://doi.org/10.1016/j.apacoust.2021.108006.
[32] Suárez L, del Mar Espinosa M. Assessment on the use of additive manufacturing technologies for acoustic applications. Int J Adv Manuf Technol 2020;109:2691–705. https://doi.org/10.1007/s00170-020-05853-2.
[33] Kuschmitz S, Ring TP, Watschke H, Langer SC, Vietor T. Design and additive manufacturing of porous sound absorbers—A machine-learning approach. Materials 2021;14:1747. https://doi.org/10.3390/ma14071747.
[34] Costa-Baptista J, Fotsing ER, Mardjono J, Therriault D, Ross A. Design and fused filament fabrication of multilayered microchannels for subwavelength and broadband sound absorption. Addit Manuf 2022;55:102777. https://doi.org/10.1016/j.addma.2022.102777.
[35] Boulvert J, Humbert T, Romero-García V, Gabard G, Fotsing ER, Ross A, Mardjono J, Groby J-P. Perfect, broadband, and sub-wavelength absorption with asymmetric absorbers: Realization for duct acoustics with 3d printed porous resonators. J Sound Vib 2022;523:116687. https://doi.org/10.1016/j.jsv.2021.116687.
[36] Zhang XH, Qu ZG. Viscous and thermal dissipation during the sound propagation in the continuously graded phononic crystals. Appl Acoust 2022;189:108606. https://doi.org/10.1016/j.apacoust.2021.108606.
[37] Opiela KC, Zieliński TG, Attenborough K. Limitations on validating slitted sound absorber designs through budget additive manufacturing. Mater Design 2022;218:110703. https://doi.org/10.1016/j.matdes.2022.110703.
[38] du Plessis A. Effects of process parameters on porosity in laser powder bed fusion revealed by X-ray tomography. Addit Manuf 2019;30:100871. https://doi.org/10.1016/j.addma.2019.100871.
[39] Williams RJ, Piglione A, Rønneberg T, Jones C, Pham M-S, Davies CM, Hooper PA. In situ thermography for laser powder bed fusion: Effects of layer temperature on porosity, microstructure and mechanical properties. Addit Manuf 2019;30:100880. https://doi.org/10.1016/j.addma.2019.100880.
[40] Dowling L, Kennedy J, O'Shaughnessy S, Trimble D. A review of critical repeatability and reproducibility issues in powder bed fusion. Mater Design 2020;186:108346. https://doi.org/10.1016/j.matdes.2019.108346.
[41] Auriault J, Boutin C. Deformable porous media with double porosity III: Acoustics. Transp Porous Media 1994;14:143–62. https://doi.org/10.1007/BF00615198.
[42] Boutin C, Royer P, Auriault J. Acoustic absorption of porous surfacing with dual porosity. Int J Solids Struct 1998;35:4709–37. https://doi.org/10.1016/S0020-7683(98)00091-2.
[43] Olny X, Boutin C. Acoustic wave propagation in double porosity media. J Acoust Soc Am 2003;114:73–89. https://doi.org/10.1121/1.1534607.
[44] Chevillotte F, Perrot C, Guillon E. A direct link between microstructure and acoustical macro-behavior of real double porosity foams. J Acoust Soc Am 2013;134:4681–90. https://doi.org/10.1121/1.4824842.
[45] Venegas R, Umnova O. Acoustical properties of double porosity granular materials. J Acoust Soc Am 2011;130:2765–76. https://doi.org/10.1121/1.3644915.
[46] Atalla N, Panneton R, Sgard F, Olny X. Acoustic absorption of macro-perforated porous materials. J Sound Vib 2001;243:659–78. https://doi.org/10.1006/jsvi.2000.3435.
[47] Sgard F, Olny X, Atalla N, Castel F. On the use of perforations to improve the sound absorption of porous materials. Appl Acoust 2005;66:625–51. https://doi.org/10.1016/j.apacoust.2004.09.008.
[48] Venegas R, Boutin C. Acoustics of permeable heterogeneous materials with local non-equilibrium pressure states. J Sound Vib 2018;418:221–39. https://doi.org/10.1016/j.jsv.2017.11.013.
[49] ISO 10534–2: Determination of sound absorption coefficient and impedance in impedance tubes; 1998.
[50] Auriault J-L, Borne L, Chambon R. Dynamics of porous saturated media, checking of the generalized law of Darcy. J Acoust Soc Am 1985;77:1641–50. https://doi.org/10.1121/1.391962.
[51] Lafarge D. Propagation du son dans les matériaux poreux à structure rigide saturés par un fluide viscothermique [Ph.D. thesis]. Université du Maine (France); 1993.
[52] Lafarge D, Lemarinier P, Allard JF, Tarnow V. Dynamic compressibility of air in porous structures at audible frequencies. J Acoust Soc Am 1997;102:1995–2006. https://doi.org/10.1121/1.419690.
[53] Gasser S, Paun F, Bréchet Y. Absorptive properties of rigid porous media: Application to face centered cubic sphere packing. J Acoust Soc Am 2005;117:2090–9. https://doi.org/10.1121/1.1863052.
[54] Perrot C, Chevillotte F, Panneton R. Bottom-up approach for microstructure optimization of sound absorbing materials. J Acoust Soc Am 2008;124:940–8. https://doi.org/10.1121/1.2945115.
[55] Lee C-Y, Leamy MJ, Nadler JH. Acoustic absorption calculation in irreducible porous media: A unified computational approach. J Acoust Soc Am 2009;126:1862–70. https://doi.org/10.1121/1.3205399.
[56] Chevillotte F, Perrot C, Panneton R. Microstructure based model for sound absorption predictions of perforated closed-cell metallic foams. J Acoust Soc Am 2010;128:1766–76. https://doi.org/10.1121/1.3473696.
[57] Perrot C, Chevillotte F, Hoang MT, Bonnet G, Bécot F-X, Gautron L, Duval A. Microstructure, transport, and acoustic properties of open-cell foam samples: Experiments and three-dimensional numerical simulations. J Appl Phys 2012;111:014911. https://doi.org/10.1063/1.3673523.
[58] Zieliński TG. Microstructure-based calculations and experimental results for sound absorbing porous layers of randomly packed rigid spherical beads. J Appl Phys 2014;116:034905. https://doi.org/10.1063/1.4890218.
[59] Zieliński TG, Venegas R, Perrot C, Červenka M, Chevillotte F, Attenborough K. Benchmarks for microstructure-based modelling of sound absorbing rigid-frame porous media. J Sound Vib 2020;483:115441. https://doi.org/10.1016/j.jsv.2020.115441.
[60] Venegas R, Boutin C. Enhancing sound attenuation in permeable heterogeneous materials via diffusion processes. Acta Acust United With Acust 2018;104:623–35. https://doi.org/10.1016/j.jsv.2017.11.013.
[61] Allard JF, Atalla N. Propagation of Sound in Porous Media: Modeling Sound Absorbing Materials. 2nd ed. Chichester: John Wiley & Sons; 2009. https://doi.org/10.1002/9780470747339.
[62] Firdaouss M, Guermond J-L, Lafarge D. Some remarks on the acoustic parameters of sharp-edged porous media. Int J Eng Sci 1998;36:1035–46. https://doi.org/10.1016/S0020-7225(98)00002-0.
[63] Cummings A. Impedance tube measurements on porous media: The effects of air-gaps around the sample. J Sound Vib 1991;151:63–75. https://doi.org/10.1016/0022-460X(91)90652-Z.
[64] Achdou Y, Avellaneda M. Influence of pore roughness and pore-size dispersion in estimating the permeability of a porous medium from electrical measurements. Physic of Fluids A 1992;4:2651–73. https://doi.org/10.1063/1.858523.
[65] Cortis A, Berryman JG. Frequency-dependent viscous flow in channels with fractal rough surfaces. Phys Fluids 2010;22:053603. https://doi.org/10.1063/1.3407659.
[66] Chevillotte F, Perrot C. Effect of the three dimensional microstructure on the sound absorption of foams: A parametric study. J Acoust Soc Am 2017;142:1130–40. https://doi.org/10.1121/1.4999058.
[67] Trinh V, Guilleminot J, Perrot C. On the sensitivity of the design of composite sound absorbing structures. Mater Design 2021;210:110058. https://doi.org/10.1016/j.matdes.2021.110058.
[68] Attenborough K. Analytical approximations for sub wavelength sound absorption by porous layers with labyrinthine slit perforations. Appl Sci 2021;11:3299. https://doi.org/10.3390/app11083299.
[69] Venegas R, Zieliński TG, Núñez G, Bécot F-X. Acoustics of porous composites. Compos Part B 2021;220:109006. https://doi.org/10.1016/j.compositesb.2021.109006.
[70] Núñez G, Venegas R, Zieliński TG, Bécot F-X. Equivalent fluid approach to modeling the acoustical properties of polydisperse heterogeneous porous composites. Phys Fluids 2021;33:062008. https://doi.org/10.1063/5.0054009.
[71] Venegas R, Boutin C, Umnova O. Acoustics of multiscale sorptive porous materials. Phys Fluids 2017;29:082006. https://doi.org/10.1063/1.4999053.
[72] Johnson DL, Koplik J, Dashen R. Theory of dynamic permeability and tortuosity in fluid-saturated porous media. J Fluid Mech 1987;176:379–402. https://doi.org/10.1017/S0022112087000727.
[73] Champoux Y, Allard J-F. Dynamic tortuosity and bulk modulus in air-saturated porous media. J Appl Phys 1991;70:1975–9. https://doi.org/10.1063/1.349482.
[74] Pride SR, Morgan FD, Gangi AF. Drag forces of porous-medium acoustics. Phys Rev B 1993;47:4964–78. https://doi.org/10.1103/PhysRevB.47.4964.
[75] Brown RJS. Connection between formation factor for electrical resistivity and fluid-solid coupling factor in Biot's equations for acoustic waves in fluid-filled porous media. Geophysics 1980;45:1269–75. https://doi.org/10.1190/1.1441123.
[76] Avellaneda M, Torquato S. Rigorous link between fluid permeability, electrical conductivity, and relaxation times for transport in porous media. Phys Fluids A 1991;3:2529–40. https://doi.org/10.1063/1.858194.
[77] ISO 9053-1:2018: Acoustics – Determination of airflow resistance – Part 1: Static airflow method; 2018.
[78] Salissou Y, Panneton R. Pressure/mass method to measure open porosity of porous solids. J Appl Phys 2007;101:124913. https://doi.org/10.1063/1.2749486.
[79] Rhodes M. (Ed.), Introduction to Particle Technology, 2nd ed. John Wiley & Sons, Chichester; 2008. doi:10.1002/9780470727102.
[80] Wang D, Fan L-S. 2 – Particle characterization and behavior relevant to fluidized bed combustion and gasification systems. In: Scala F, editor. Fluidized Bed Technologies for Near-Zero Emission Combustion and Gasification, Woodhead Publishing Series in Energy. Woodhead Publishing; 2013. p. 42–76. https://doi.org/10.1533/9780857098801.1.42.

[81] Utsuno H, Tanaka T, Fujikawa T, Seybert AF. Transfer function method for measuring characteristic impedance and propagation constant of porous materials. J Acoust Soc Am 1989;86:637–43. https://doi.org/10.1121/1.398241.
[82] Iwase T, Izumi Y, Kawabata R. A new measuring method for sound propagation constant by using sound tube without any air spaces back of a test material. In InterNoise98, Christchurch, New Zeland; 1998. pp. 1265–1268.
[83] Salissou Y, Panneton R, Doutres O. Complement to standard method for measuring normal incidence sound transmission loss with three microphones. J Acoust Soc Am 2012;131:EL216–22. https://doi.org/10.1121/1.3681016.
[84] Panneton R, Olny X. Acoustical determination of the parameters governing viscous dissipation in porous media. J Acoust Soc Am 2006;119:2027–40. https://doi.org/10.1121/1.2169923.
[85] Olny X, Panneton R. Acoustical determination of the parameters governing thermal dissipation in porous media. J Acoust Soc Am 2008;123:814–24. https://doi.org/10.1121/1.2828066.
[86] Jaouen L, Gourdon E, Glé P. Estimation of all six parameters of johnson-champoux-allard-lafarge model for acoustical porous materials from impedance tube measurements. J Acoust Soc Am 2020;148:1998–2005. https://doi.org/10.1121/10.0002162.
[87] Venegas R. Microstructure influence on acoustical properties of multiscale porous materials [Ph.D. thesis]. University of Salford, Salford, United Kingdom; 2011.
[88] Zieliński TG. Normalized inverse characterization of sound absorbing rigid porous media. J Acoust Soc Am 2015;137:3232–43. https://doi.org/10.1121/1.4919806.
[89] Cuenca J, Gøransson P, De Ryck L, Lähivaara T. Deterministic and statistical methods for the characterisation of poroelastic media from multi-observation sound absorption measurements. Mech Syst Signal Process 2022;163:108186. https://doi.org/10.1016/j.ymssp.2021.108186.
[90] Roncen R, Fellah ZEA, Ogam E. Addressing the ill-posedness of multi-layer porous media characterization in impedance tubes through the addition of air gaps behind the sample: Numerical validation. J Sound Vib 2022;520:116601. https://doi.org/10.1016/j.jsv.2021.116601.
[91] Boutin C, Geindreau C. Estimates and bounds of dynamic permeability of granular media. J Acoust Soc Am 2008;124:3576–93. https://doi.org/10.1121/1.2999050.
[92] Boutin C, Geindreau C. Periodic homogenization and consistent estimates of transport parameters through sphere and polyhedron packings in the whole porosity range. Phys Rev E 2010;82:036313. https://doi.org/10.1103/PhysRevE.82.036313.